Signal Processing Systems
Mekelweg 4,
2628 CD Delft
The Netherlands
https://sps.ewi.tudelft.nl/

SPS-2023-5472776

M.Sc. Thesis

Location Estimation of Atrial Activity from Epicardial Electrogram measurements

Anjali Suresan

Faculty of Electrical Engineering, Mathematics and Computer Science **Delft University of Technology**

Location Estimation of Atrial Activity from Epicardial Electrogram measurements

Thesis report

by

Anjali Suresan

in partial fulfillment of the requirements for the degree of

Master of Science
in Electrical Engineering

at the Delft University of Technology
to be defended publicly on August 30, 2023 at 10:00 AM

Thesis committee:

Chair:	Dr. Ir. Rob Remis
Supervisors:	Dr. Ir. Rob Remis
	Dr. Ir. Richard Hendriks
External examiner:	Dr. Clementine Boutry
Place:	Faculty of Electrical Engineering, Delft
Project Duration:	November, 2022 - August, 2023
Student number:	5472776

An electronic version of this thesis is available at `http://repository.tudelft.nl/`.

Delft University of Technology

Delft University of Technology
Department of
Microelectronics

The undersigned hereby certify that they have read and recommend to the Faculty of Electrical Engineering, Mathematics and Computer Science for acceptance a thesis entitled **"Location Estimation of Atrial Activity from Epicardial Electrogram measurements"** by **Anjali Suresan** in partial fulfillment of the requirements for the degree of **Master of Science**.

Dated: 30.08.2023

Chairman: _____
Dr. Ir. Rob Remis

Advisors: _____
Dr. Ir. Rob Remis

_____
Dr. Ir. R. C. Hendriks

Committee Member: _____
Dr. Clementine Boutry

Abstract

Atrial Fibrillation (AF) is a cardiac arrhythmia that occurs due to the initiation of electrical impulses in the heart in an uncoordinated manner, giving rise to a disorganized and rapid heartbeat. The progression of AF over time can lead to complications such as stroke and heart failure. Catheter ablation is an established treatment protocol adopted to eliminate AF triggers and restore normal sinus rhythm in patients. To improve the success rates of ablation procedures, mapping and localizing the regions in the heart that give rise to uncoordinated impulses is crucial. This work focuses on obtaining a visual estimate of the location of irregular electrical activity within a volume domain of cardiac tissue using epicardial electrogram measurements.

A straightforward, effective and computationally fast backprojection imaging method is proposed that provides an indication of the regions in a given volume of cardiac tissue that exhibit prominent irregular atrial activity. The chosen volume is subdivided into non-overlapping voxels, and the standard electrogram signal model is discretized to a matrix multiplication form. The inverse problem of reconstructing the transmembrane current distribution in the volume is solved using the epicardial electrogram readings obtained from the surface and the inverse distances matrix containing the inverse of the distances from each electrode to each voxel within the volume domain. The generated backprojection images are visualized to estimate the location (x and y coordinate information) and depth of irregular atrial activity in the volume. To improve the accuracy of localization while maintaining the computationally fast nature of the proposed solution, Singular Value decomposition (SVD) of the inverse distances matrix is proposed for the transmembrane current reconstruction. The obtained visual estimates can guide ablation procedures, making them more targeted, and reducing the need for repeat ablation procedures due to AF recurrence.

Acknowledgements

This thesis marks the completion of my MSc in Electrical Engineering with a specialization in Signals and Systems at the Delft University of Technology. My Master's journey and this research would not have been possible without the encouragement and support of many individuals.

First and foremost, I thank Dr. Rob Remis and Dr. Richard Hendriks for being my thesis supervisors. Their timely guidance and suggestions were crucial in helping me explore different research directions to materialize the thesis. I thank Dr. Rob Remis for patiently guiding me with the thesis report and providing valuable feedback on my work. I am also grateful to Dr. Clementine Boutry for being a part of my graduation committee.

Secondly, I would like to show my appreciation to Dr. B. Abdi, whose doctoral dissertation and work on Atrial fibrillation fingerprinting helped me understand the foundation of this project and provided me with great insight to pursue this research topic.

Lastly, I am incredibly grateful to my family and friends in India and Delft for their unwavering support and constant motivation. Thank you for believing in me during the low moments.

Anjali Suresan
Delft, The Netherlands
30 August 2023

Contents

List of Figures

List of abbreviations

AF Atrial Fibrillation

SA Sino Atrial

AV Atrioventricular

AP Action potential

ECG Electrocardiogram

EGM Electrogram

SR Sinus Rhythm

AA Atrial Activity

VA Ventricular Activity

TMS Template Matching and Subtraction

ICA Independent Component Analysis

MVDR Minimum Variance Distortionless Response

EBE Extended Bipolar Electrode

SVD Singular Value Decomposition

1 Introduction

1.1 Research Motivation

Atrial Fibrillation (AF) is the most commonly encountered sustained cardiac arrhythmia [1]. AF is characterised by highly irregular electrical activity in the heart and primarily affects the elderly population. An estimated 12.1 million people in the United States will have AF by 2030 [2]. In the Netherlands alone, as of December 2022, 360,000 people were known to have AF, and there are an estimated 80,000 undetected cases [3]. Atrial Fibrillation can ultimately lead to complications such as stroke, blood clots, heart failure, and death. The risk of complications increases with time. Therefore, preventing the progression of the arrhythmia is crucial.

Current treatment methods for atrial fibrillation include using anti-arrhythmic drugs to control the heart rate or rhythm control strategies such as cardioversion or radiofrequency catheter ablation [4]. These methods help to restore and maintain sinus rhythm.

The duration of AF episodes has clinical relevance since the effectiveness of therapy methods depends on the type of AF being dealt with. AF can be broadly categorized into four types: Paroxysmal AF is characterized by brief events that can repeat and usually stop spontaneously within seven days. Persistent AF lasts for more than a week and usually requires treatment to regulate the heartbeat. Longstanding persistent AF occurs when the abnormal heart rhythm lasts for over a year without improvement. Permanent AF is the last stage that does not get better, and no further attempts are made to restore sinus rhythm. Atrial fibrillation often proceeds from paroxysmal to persistent to long-term, especially without therapy [5].

Catheter ablation is a minimally invasive technique widely adopted in the treatment of AF. It involves inserting a specially designed catheter into the left atrium and applying radiofrequency energy to the heart muscle to cauterize the sites that trigger atrial fibrillation. A single treatment eliminates paroxysmal atrial fibrillation in 70-75 % of individuals. The overall success rate rises to about 85-90 % when the operation is repeated on patients who still have atrial fibrillation after the initial procedure. A single procedure effectively eliminates persistent atrial fibrillation in approximately 50 % of patients [6].

Focused treatment leads to less recovery time and lower chances of recurrence of AF in patients. The mapping of the areas in the heart that cause the unsteady rhythm is crucial for the success of the ablation procedure and to prevent the patient from having to undergo multiple ablation procedures before they get relief. Obtaining an estimate of the location in the heart at which irregular atrial activity occurs and initiates the AF can be valuable for understanding the underlying mechanism of why AF occurs and also for localizing and neutralizing the diseased tissue in the heart that essentially act as the

origin of the irregular electrical activity causing AF. Identifying these trigger sites would subsequently improve the success rates of guided ablation procedures and pave the way for patient-tailored therapy.

The main targets in the ablation procedure are the AF onset locations and drivers responsible for its perpetuation. In this thesis, improving the outcome of guided catheter ablation by estimating the location where irregular atrial activity is observed within a volume of heart tissue using recorded electrogram measurements is of particular interest. A straightforward, efficient, and computationally fast imaging method is proposed to reconstruct the electrical activity distribution inside a volume domain. This is useful for determining the site of the irregular atrial activity within the volume and providing a visual estimate of the location of the diseased tissue that can be further analyzed to guide ablation procedures.

1.2 Research Objective

The research objective is to estimate the region where the irregular atrial activity is prominent within a volume domain using an imaging method that is simple, fast, and not computationally complex. Visually localizing the regions within the atria that exhibit irregular electrical activity can be valuable information for the medical fraternity to study the trigger sites responsible for AF and guide ablation procedures to eliminate these triggers. To this end, the use of a backprojection imaging technique is explored in this thesis for reconstructing the transmembrane current distribution within a volume domain. Specifically, the primary research question investigated is as follows: Given electrogram data recorded using an electrode array placed on the epicardial surface of the heart, how can the atrial activity location and depth within a specific volume domain be determined using a simple imaging method?

1.3 Thesis Outline

The thesis report is organized into six chapters. In this current chapter, an introduction to the main research problem at hand is provided and the research objective is outlined. The subsequent chapters are organized as follows:

- Chapter 2 gives an overview of the necessary background knowledge. The context of the thesis is explained, and the previous research and state-of-the-art methods used in the study of AF are summarised.
- Chapter 3 explores the discretization of the standard electrogram signal model to a matrix multiplication form and introduces the baseline simulation setup used for volume imaging.
- Chapter 4 describes and discusses the generation of backprojection images for obtaining a visual estimate of the atrial activity location in a volume domain. An

analysis is carried out to determine the ability of the backprojection image to spatially resolve two closely spaced sites of irregular atrial activity within the volume. For the depth estimation, an angled orientation of the electrode array placed within the volume of cardiac tissue is introduced.

- In Chapter 5, to further improve the accuracy of location estimation in the backprojection images, a Singular Value Decomposition (SVD) of the inverse distances matrix is performed for the reconstruction of the transmembrane current distribution.
- Chapter 6 summarises the contributions of the thesis and proposes directions for future research.

2 Background

In this chapter, we provide an overview of the pathway followed by an electrical impulse in the heart and an introduction to the most common type of cardiac arrhythmia called Atrial fibrillation. A discussion of the methods for measuring the electrical activity in the heart follows, with a particular emphasis on electrograms that are used further in this study. A summary of the mathematical models used to define electrograms is provided next, followed by a brief overview of the preprocessing of the electrogram signals for ventricular interference removal and the state-of-the-art methods used for conductivity estimation from the electrogram data.

2.1 Electrical Conduction in the heart

The heart consists of four chambers: the two upper chambers called the atria and the two lower chambers called the ventricles. The heart pumps blood throughout the body in successive cardiac cycles using these four chambers. The chambers on the right deliver oxygen-depleted blood to the lungs, while the left atria and left ventricle deliver oxygen-rich blood to the body. A series of electrical impulses generated and conducted by the cardiac conduction system gives rise to the cardiac cycle.

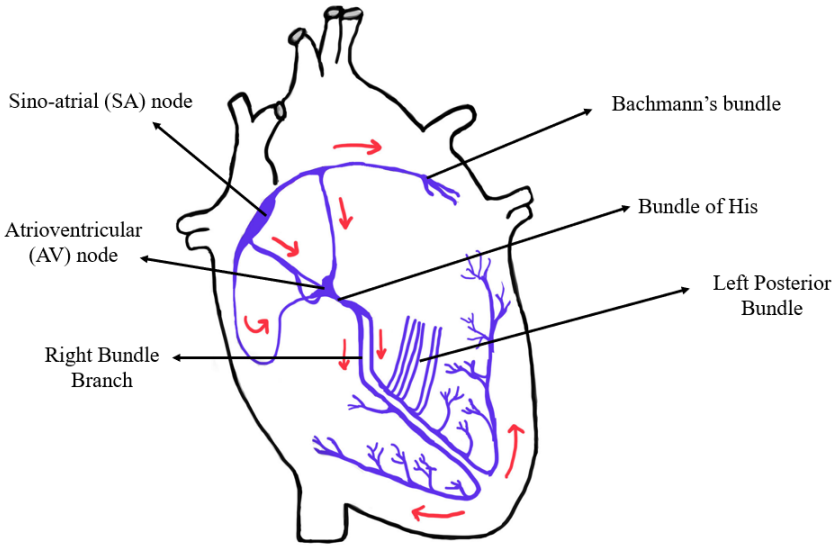

Figure 2.1: Electrical conduction system of the heart.

Figure 2.1 shows the electrical conduction system of the heart. At the start of each cardiac cycle, an impulse is generated by a collection of cells at the sinoatrial (SA) node, located on the right atrial wall. The SA node is referred to as the anatomical pacemaker. These impulses pass through the Bachman's bundle and to the atrioventricular (AV) node via specific electrical pathways. The atrial muscles contract as a result of the propagation of these electrical impulses. The impulses are delayed briefly at the AV node to ensure the blood is completely expelled from the atria and into the ventricles. The electrical impulse then propagates to the ventricles via the bundle of His divided into two pathways called the bundle branches. The contraction of the ventricles, that occurs next, represents a heartbeat [7]. The red arrows in Figure 2.1 indicate the pathway followed by the impulse from the atria to the ventricles.

The electric impulse propagation in the heart involves the generation of Action potential (AP) by cells at the SA node and their conduction across cells through inter-cellular gap junctions [8]. The cell membrane has a resting potential of -90mV. During AP, the cell membrane potential undergoes a sequence of changes starting with a depolarization phase characterized by a rapid rise in cell membrane potential. This phase is followed by a plateau and subsequent repolarization phase where the membrane potential falls to the resting potential. Once the activation is initiated, a certain period of time called the refractory period has to pass before the cell can be activated again [9]. Figure 2.2 gives a representation of the different phases that the cell membrane potential undergoes during AP. As the cells in the SA node undergo the depolarization phase, AP generation is initiated in the neighboring cardiac cells causing them to contract and triggering the initiation of AP in their neighboring cells. In this way, the depolarization wave propagates through the whole heart.

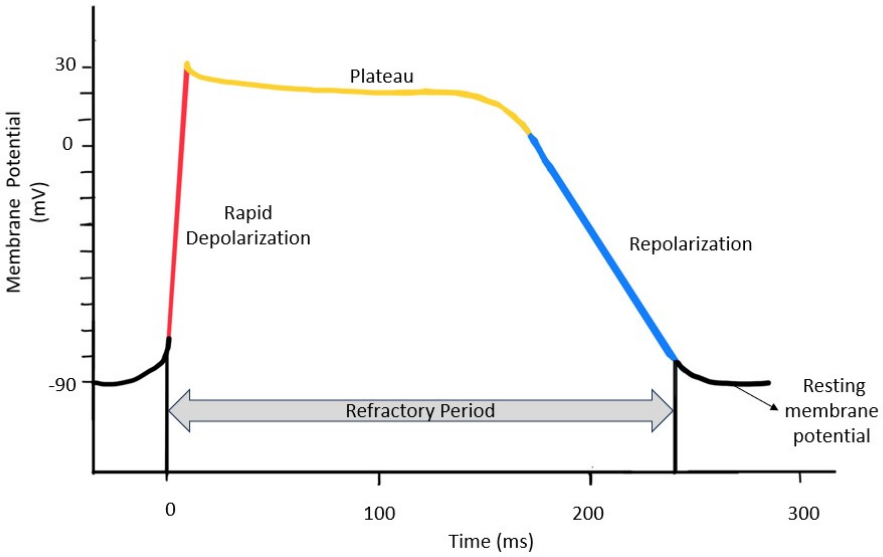

Figure 2.2: Phases of cardiac Action Potential.

2.2 Cardiac Arrhythmia and Atrial Fibrillation

Cardiac arrhythmia occurs when the electrical signals that coordinate the heartbeat do not function as expected. The faulty signals resulting from abnormalities in the conductive system of the heart can lead to tachycardia (fast beating), bradycardia (slow beating), or an irregular heartbeat [10]. Atrial Fibrillation is the most common arrhythmia encountered in clinical practice and causes rapid uncoordinated heart rate. The severity of AF largely varies among patients. AF can be temporary but can also be associated with heart failure, stroke, and mortality. The incidence of AF could be due to several factors such as increased age or obesity [11]. During AF, electrical impulses may be initiated at different sites within the atria causing it to contract in a disorganized way. The signals travel through the walls of the atria, stimulating the atria at an abnormally high rate of 300 to 600 beats per minute and causing it to quiver or fibrillate. The abnormal signals eventually propagate to the ventricles and cause them to contract erratically. In this condition, the atrial and ventricular activity is not coordinated as it would be in the normal sinus rhythm. The abnormal beating of the atria could cause ineffective pumping of blood from the atria to the ventricles, giving rise to the possibility of blood clots in the bloodstream that increases the risk of stroke [12].

2.2.1 Possible mechanisms leading to AF

Several studies have attempted to determine the complex pathophysiology of AF and the underlying mechanism that leads to the onset and persistence of AF. The precise mechanism that gives rise to AF is not conclusively established and is under debate. However, reentry, rotors, ectopic foci, breakthroughs, and multiple wavelets are the mechanisms most commonly considered to explain the initiation of AF [13]. Figure 2.3 gives a schematic representation of the different AF mechanisms.

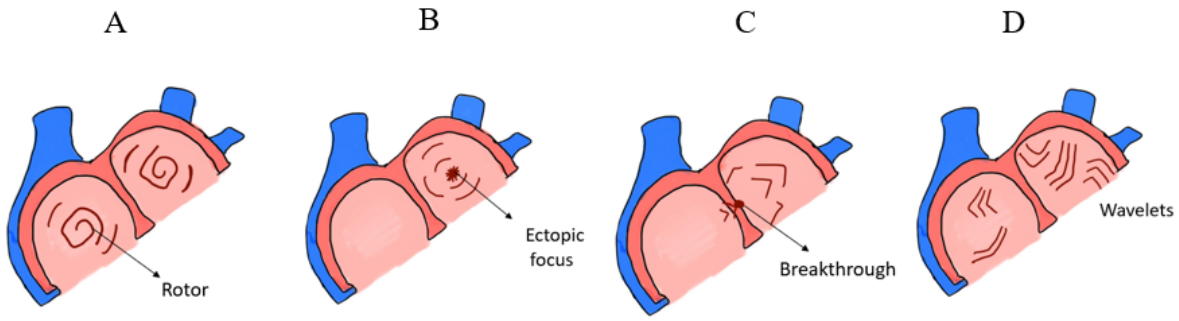

Figure 2.3: AF mechanisms.

The reentry mechanism occurs when a circuit is created within the myocardium of the heart by an activation wave that travels in a circular path around an anatomical structure, such as scarred tissue, and does not die out. A rotor is a spatially localized driver. In the

case of a rotor, the action potential propagates around an unexcited core. The rotor is a type of functional reentry pattern of activation that is not related to anatomical structures and can propagate through tissue [13], [14]. Some studies also attribute the initiation of AF to spontaneously fired Pulmonary Vein (PV) and non-PV foci. These ectopic foci release electrical stimuli different from the expected conduction paths, interfering with sinus activity [15]. Besides ectopic foci, focal fibrillatory waves can also occur due to the breakthrough mechanism. The breakthrough mechanism can happen due to asynchronous wave propagation in the endo and epicardial layer of the atria and can be responsible for AF initiation [16]. Lastly, the multiple wavelet mechanism occurs when the wave propagating through the tissue breaks into multiple wavelets due to collision with an anatomical barrier. The multiple wavelets can subsequently give rise to more wavelets spreading in different directions, leading to the chaotic electrical activity observed during AF.

These mechanisms are not mutually exclusive and can co-exist [13]. Regardless of the exact mechanism that gives rise to AF, the localization of the regions where the irregular activity is prominent can be crucial for identifying and eliminating AF triggers and determining the treatment protocol in patients.

2.2.2 Catheter Ablation

Ablation is a treatment method adopted to eliminate AF triggers and restore sinus rhythm in patients with AF. It is a well-established treatment protocol with positive outcomes for patients with an otherwise normal cardiac function, exhibiting symptomatic AF that is resistant to drug therapy, and for patients with heart failure [17]. This minimally invasive procedure involves the insertion of a catheter through the vasculature for the application of radio-frequency energy, typically for 60 seconds, to burn a small area of heart tissue that is diseased. This process disrupts the conduction of the abnormal electrical signals in the heart that give rise to the uncoordinated heartbeat. Sometimes, the ablation procedure is done when a patient has open heart surgery. Although ablation is a widely adopted treatment method for AF, there is a high risk that the AF is not permanently eliminated after the procedure and could recur in a few months [18]. Recording the electrical activity in the heart to identify regions where the irregular activity is prominent can guide the ablation procedure and make it more targeted.

2.3 Methods for measurement of Electrical Activity in the heart

Measuring the electrical activity in the heart is important for identifying abnormalities in its functioning. Electrocardiography, giving rise to the electrocardiogram (ECG or EKG), is a non-invasive method most commonly used to study cardiac electrical activity. In this method, a set of electrodes placed on the body surface measure the electrical signals generated by the heart. An ECG records the spatial average of the activity of all heart cells. Often for diagnosis, a 12-lead ECG is used, where 12 electrodes are placed on the surface

of a patient's body in a configuration such that the received signals have less correlation with each other [19].

Another method of obtaining measurements of cardiac electrical activity is Electrography. This invasive method uses electrode arrays placed directly on the heart tissue instead of the body surface [20]. The measurements are recorded during open heart surgery or by placing a catheter inside the heart. The measured signals called electrograms (EGMs) provide more localized information about specific sites in the heart instead of information about the heart as a whole. However, obtaining the EGM data has limitations since it can be recorded only under specific conditions during heart surgery and is a highly invasive method.

Epicardial electrograms (EGMs) recorded on the outermost layer of the heart during open heart surgery are used to study AF since, in conventional surface ECGs, the atrial signal is weak and easily corrupted by noise. EGMs also have the advantage of higher spatial resolution and the possibility of using multiple electrodes to gather information over space and time to analyze AF. Figure 2.4 shows a comparison of the ECG and EGMs recorded at one electrode during Sinus Rhythm (SR) and Atrial Fibrillation (AF).

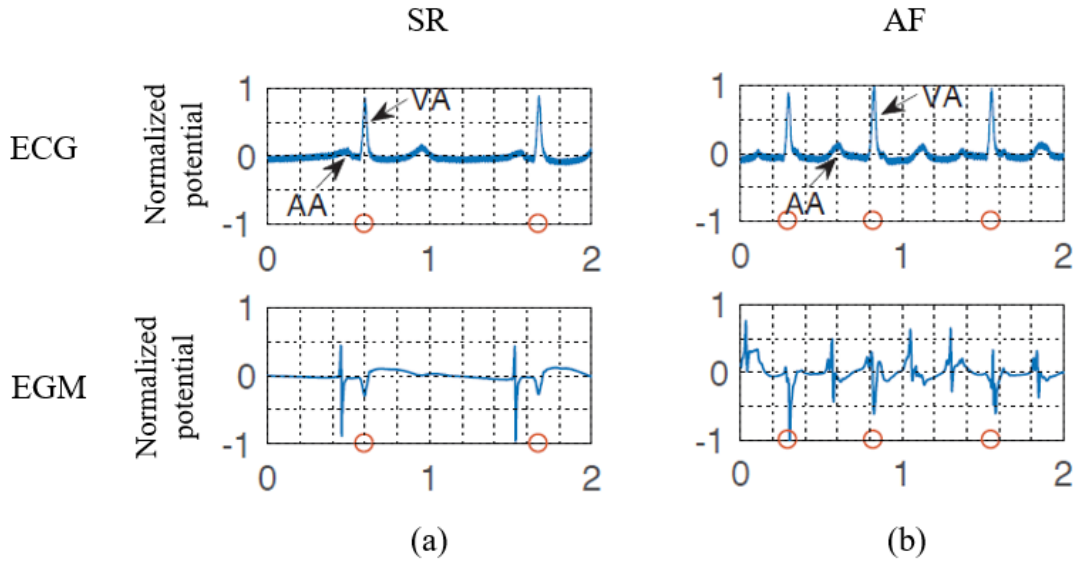

Figure 2.4: (a) The ECG and EGM recorded during sinus rhythm. (b) The ECG and EGM recorded during AF (adapted from [21]).

In the ECG measurements in the top row in Figure 2.4, the lower peaks correspond to the Atrial Activity (AA). The higher peaks that follow the AA indicate Ventricular activity (VA). The red circles in all plots indicate the VA peaks. It is observed that, in the ECG measurements, the VA is more pronounced, and the AA appears weak. However, in the EGM measurements, this is reversed. The AA is more pronounced in the EGM, although it is short in duration. This difference arises due to the spatial averaging that occurs when the atrial signal is measured on the body surface in the case of an ECG compared to the direct measurement on the epicardial surface in the EGM.

2.4 Electrogram Data

There is a need for analysing EGMs to understand the underlying mechanism that gives rise to AF. This can also increase the success rate in guided ablation therapy by localizing regions of the atria that initiate AF. One method of obtaining these electrograms can be with the use of high-resolution electrode mapping techniques. With this intra-operative method, electrograms are captured from multiple epicardial sites of the human atria in a parallel manner during open heart surgery [20]. Mapping is sequentially done using an electrode array consisting of 192 electrodes to cover the left and right atria. In the research highlighted in [20], a total of 1728 recording sites were mapped within a short recording time of 9 minutes. The recorded electrograms give highly localized spatial and temporal information of the electrical activity at multiple regions of the atria. The atrial mapping approach thus, makes it possible to identify vulnerable sites that are responsible for the initiation and persistence of AF.

Another method of obtaining the electrogram data to study AF is by generating simulated AF from a computer model. The use the MRI images of the human heart to develop a realistically sized computer model of the atria is explored in [22]. The domain is a three-dimensional monolayer owing to the thin walls of the atria. The location of major blood vessels and valves are represented as obstacles in the model. The advantage of the approach is significant reduction in computation load and the ability to simulate longer atrial arrhythmias. The generated model outputs both the transmembrane and extracellular potential. AF is simulated using a single site burst pacing protocol. In this method, a 20 Hz stimulation was applied to a 3 mm^2 area at the SA node for several seconds. Due to the refractory period in the action potential propagation, the stimuli applied fail to generate a propagating wavefront. However, after several beats, the burst pacing degenerates into multiple wavelets, giving rise to Simulated AF. The simulated AF is thus seen as independent wavelets propagating randomly in the tissue in the absence of external stimulation. In most cases, the number of wavelets on the surface was found to vary in the range of 1 to 7 and it was consistent with the experimental models of AF.

2.5 Mathematical models

In order to understand the obtained electrogram measurement data and determine the electrophysiological characteristics of the cardiac tissue and the underlying mechanism of AF, it is important to make use of mathematical models of the electrical activity in cardiac tissue. An overview of mathematical models used to define electrical activity in the heart is provided next.

2.5.1 Monodomain and Bidomain Model

Mathematical models of the human heart are reviewed in [23]. A specific distinction is made in terms of the bidomain and monodomain models. The bidomain model represents the

cardiac tissue as a continuous approximation with intracellular and extracellular domains separated by a cell membrane. The monodomain model is a simplified version of the bidomain model. It assumes that the anisotropy of the intracellular and extracellular domains is the same and the conductivity in the extracellular space is proportional to the intracellular space. This can be written as

$$G_e = \lambda G_i, \tag{2.1}$$

where λ is a scalar that relates the extracellular conductivity G_e to the intracellular conductivity G_i. A comparison of the patterns of action potential propagation simulated using the two models showed that the pattern obtained using the monodomain model was identical to that received with the bidomain model in the absence of external stimuli [24].

2.5.2 Action Potential Model

The need to understand the electrical behaviour gave rise to complex models such as the Courtemanche model of a single atrial cell [25]. In this model, the cell membrane divides the intracellular and extracellular domains, and is modelled as a capacitor connected in parallel to variable resistance and voltage sources representing the ionic channels and driving forces. Figure 2.5 gives a visualization of an equivalent circuit of the AP model.

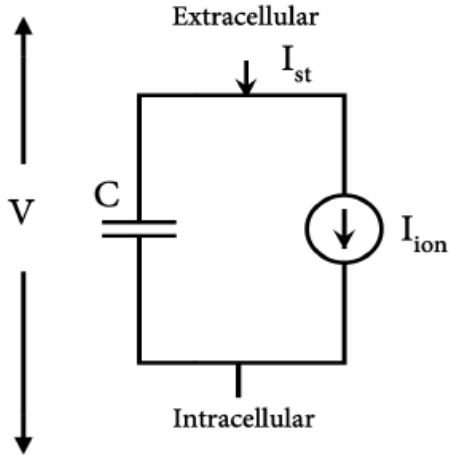

Figure 2.5: Equivalent circuit of AP model [26].

The capacitive current through the cell membrane is given as,

$$C\frac{\partial V(t)}{\partial t} = I_{st}(t) - I_{ion}(t, V) \tag{2.2}$$

where $V(t)$ is the transmembrane potential at time t, C is the total membrane capacitance, $I_{st}(t)$ is the external stimulus current and $I_{ion}(t, V)$ is the total ionic current that includes all the ionic and pump currents through the membrane [25].

2.5.3 Electrogram model

The standard electrogram signal model is addressed in [22]. This model relates the atrial electrogram recorded by an electrode array placed on the epicardium to the transmembrane current and is given by

$$\boldsymbol{\phi}(\mathbf{y},t) = \frac{1}{4\pi\sigma_e}\int_{\mathbf{x}\in A_0}\frac{I_{tm}(\mathbf{x},t)}{||\mathbf{y}-\mathbf{x}||}dA(\mathbf{x}). \tag{2.3}$$

The electrogram $\boldsymbol{\phi}(\mathbf{y},t)$ is measured at time t by an electrode at the location $\mathbf{y}$. The constant extracellular conductivity is given as σ_e. The modelled cells are considered to be located in the area A_0. This model acts as a baseline model to generate the simulated electrogram measurements for further analysis in this thesis. The electrogram signal model and its discretization process is discussed in detail in Chapter 3.

2.6 Removal of ventricular activity

Pre-processing of the electrogram data for removal of noise and artefacts is needed before analysis can be performed. Strong far-field ventricular activities are present in atrial electrograms. During Sinus Rhythm (SR), the atrial and ventricular activity (VA) is temporally separated. During AF, the atrial and ventricular activities overlap due to the rapid beating of the atria and hence, removal of the ventricular activity interference is desired for the research on atrial fibrillation. The algorithms used for VA removal can be largely divided into three categories:

- Template matching and subtraction (TMS): This method involves computing the average ventricular activity followed by subtracting the computed VA from the raw measurements. For example, surface ECG recordings can be used to identify VA in the unipolar EGMs [27]. A robust template of VA is constructed and then subtracted from the EGM to reveal the AF in the residual signal. A widely used TMS technique to dissociate the atrial and ventricular activities in electrocardiograms is Average beat subtraction [28].
- Blind source separation approach: This group of methods is based on the assumption that AA and VA are uncorrelated, orthogonal and statistically independent over time and space in multichannel recordings. Independent component analysis (ICA) is an example of such a technique proposed to solve the problem [29].
- Adaptive filtering based on a VA reference: The reference is often obtained from a surface ECG recording. Adaptive Ventricular cancellation (AVC) discussed in [30], however, fails to give a stable result due to its dependence on a reference recording.

A perfect estimate of the pure AA recording is not achieved using these methods as the AA and VA recordings are partially correlated over space and time and share overlapping components in the time and frequency domain. A novel framework for VA and AA separation by means of interpolation and subtraction followed by low rank and Sparse matrix decomposition is proposed in [31]. A simultaneously recorded ECG signal is used

as reference to remove VA containing segments. These are replaced by spline interpolation applied to remaining samples. A data matrix is modelled as the sum of a component containing the VA and a component containing the AA that coincides with the VA segment. Decomposing the data matrix gives rise to an underdetermined blind source separation problem. Prior knowledge of the two sources is employed to give a convex optimization problem that is solved using ADMM (Alternating direction method of multipliers). The method proposed outperforms TMS and ICA, particularly when the VA is less regular.

Another method for estimation of Atrial Activity in synthetically generated EGMs containing VA and different degrees of AF using a beamforming approach, common in the field of array signal processing, is discussed in [32]. Two different beamformers are proposed to solve the AA estimation problem: the Extended Bipolar electrode (EBE) beamformer and the minimum variance distortionless response (MVDR) beamformer. It is found that the MVDR outperforms the EBE for data sets with low degree of AF and the EBE performs better in scenarios with higher degrees of AF. The performance of both beamformers is improved for a higher number of electrodes.

2.7 Conductivity Estimation

Various parameters are estimated from electrograms to characterize its properties, understand the wave propagation in the tissue and study AF. A simplified electrogram model is developed in [33]. The simplified forward model reduces computational load while still being physiologically accurate enough. The model is represented in a compact matrix form that shows the linear dependence of the electrogram data on the tissue conductivity vector. This enables estimation of the conductivity map from the recorded electrogram data. The ill-posed inverse problem of tissue conductivity estimation could thus be solved efficiently.

Parameter estimation from recorded electrogram data gives insight into tissue abnormality. A novel method using graph signal processing techniques and short time Fourier transform has been presented in [21]. The graph time spectral analysis framework exploits the information present in the spatial domain of the clinical data obtained from the atrial mapping approach [20]. A cross power spectral density matrix model of the EGMs is also developed for joint parameter estimation using Confirmatory Factor Analysis. The target parameters considered are the activation time, anisotropy ratio and conductivity to analyse abnormalities in the cardiac tissue.

This chapter gave an overview of the necessary background knowledge on cardiac arrhythmias, atrial fibrillation, electrograms and the mathematical models used for simulating electrograms. This information forms the basis for the upcoming chapters in this thesis. An introduction to the state-of-the-art methods for removal of ventricular activity and conductivity estimation was also briefly discussed.

In the following chapter, we start with the electrogram signal model and discretize it to a matrix multiplication form. This facilitates the generation of backprojection images for estimating the location of atrial activity within a volume domain and can provide important visual estimates for determining catheter placements in guided ablation procedures.

Discretization of Standard Electrogram Signal Model

3

A signal model of the electrogram data recorded by an electrode array placed on the epicardial surface of the heart can be beneficial for estimating the locations where atrial activity is prominent within a volume domain of monolayer cardiac tissue. Subsequently, the location estimate can be used for determining the catheter placement locations in guided ablation procedures and improving the success rate of these procedures. In this chapter, we aim to discretize the standard electrogram signal model in order to develop a matrix model for the electrogram data and gain further insight into the estimation process. A clearly defined volume domain subdivided into non-overlapping voxels is considered for the discretization process. The matrix containing the inverse distances from the electrodes to the voxels plays a key role in the generation of the electrogram data and in the subsequent imaging process. Finally, the simulation setup used for the reconstruction of the transmembrane current distribution and the volume imaging is also discussed in detail.

3.1 Derivation of Matrix Multiplication Model

Cardiac cells can be modelled as conductive surfaces through which current propagates as a result of changes in the transmembrane voltages and the electrodynamic interactions among the cells. The electrogram records the changes in potential of the cells located in the vicinity of an electrode placed on the epicardial surface for atrial mapping. Current source approximation for a large volume conductor can be used to model the electrogram as [22]

$$\phi_m(\mathbf{x}, t) = \frac{1}{4\pi\sigma_e} \int_{\mathbf{x}' \in A} \frac{I_{tm}(\mathbf{x}', t)}{||\mathbf{x} - \mathbf{x}'||} d\mathbf{x}'. \tag{3.1}$$

Vectors $\mathbf{x}$ and $\mathbf{x}'$ indicate the position of the electrodes and the cells respectively. The domain where the current is present, giving rise to electrical activity, is denoted by A. σ_e is the constant extracellular conductivity and $I_{tm}(\mathbf{x}', t)$ is the transmembrane current per unit area at location $\mathbf{x}'$ and at time t.

In general, the region where the current is present is not known. However, we can introduce a large and conveniently chosen imaging domain $\mathbb{D}_{im}$ such that $A \subset \mathbb{D}_{im}$. The current is non-existent at all points outside A. With the introduction of the larger imaging domain, the integral can now be written as:

$$\phi_m(\mathbf{x}, t) = \frac{1}{4\pi\sigma_e} \int_{\mathbf{x}' \in \mathbb{D}_{im}} \frac{I_{tm}(\mathbf{x}', t)}{||\mathbf{x} - \mathbf{x}'||} d\mathbf{x}'. \tag{3.2}$$

To model the measurement process, a finite space discretized version of the above standard electrogram model is used. A set of N_e sensors are positioned on a plane at positions

$\mathbf{x}_m \in \mathbb{R}^3$ with $m \in [1, 2, ...N_e]$. The rectangular imaging domain $\mathbb{D}_{im}$ is considered which is subdivided into N identical non-overlapping voxels, each occupying a subdomain $\mathbb{D}_n$ such that

$$\mathbb{D}_{im} = \bigcup_{n=1}^{N} \mathbb{D}_n. \tag{3.3}$$

Equation (3.2) can now be rewritten as:

$$\phi_m(\mathbf{x}_m, t) = \frac{1}{4\pi\sigma_e} \sum_{n=1}^{N} \int_{\mathbf{x}' \epsilon \mathbb{D}_n} \frac{I_{tm}(\mathbf{x}', t)}{||\mathbf{x}_m - \mathbf{x}'||} d\mathbf{x}'. \tag{3.4}$$

The integral in Eq. (3.4) is discretized using the midpoint rule by replacing the integral with the value of the integrand at the midpoint of the voxel multiplied by the area of the voxel. The voxels have identical side lengths and consequently the same area a. The position vector corresponding to the midpoint of the voxels is denoted as $\mathbf{x}'_n \in \mathbb{R}^3$ with $n \in [1, 2, ...N]$. Figure 3.1 shows the setup used for the discretization process. The distance $x_{m,n}$ from the m^{th} electrode to the n^{th} voxel is given as,

$$x_{m,n} = ||\mathbf{x}_m - \mathbf{x}'_n|| = \sqrt{(x_m - x'_n)^2 + (y_m - y'_n)^2 + (z_m - z'_n)^2}. \tag{3.5}$$

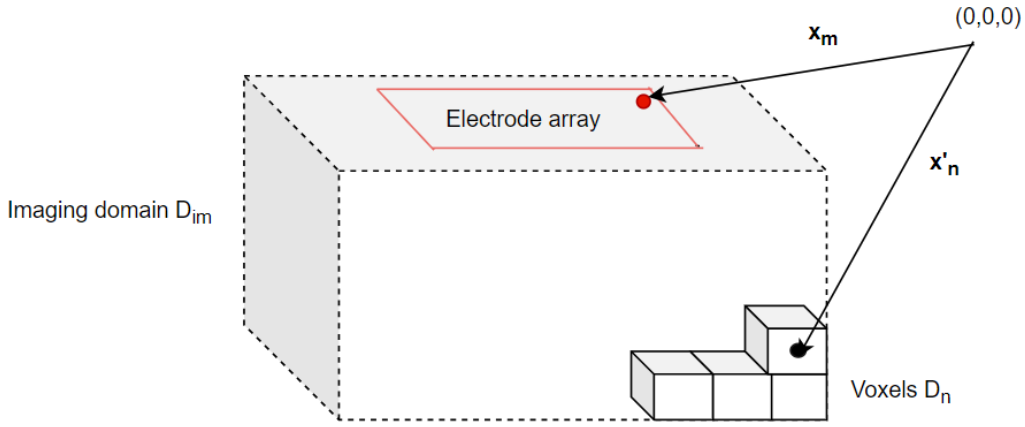

Figure 3.1: The domain $\mathbb{D}_{im}$ used for imaging is subdivided into voxels, each with a domain $\mathbb{D}_n$. The position vectors of the midpoint of the n^{th} voxel is given by $\mathbf{x}'_n$ and the position vector of the m^{th} electrode is given by $\mathbf{x}_m$.

The resulting discretized form of the electrogram model is:

$$\phi_m(t) = \frac{a}{4\pi\sigma_e} \sum_{n=1}^{N} \frac{I_{tm}(\mathbf{x}'_n, t)}{||\mathbf{x}_m - \mathbf{x}'_n||}. \tag{3.6}$$

The final discretized data equation in a matrix multiplication model is given as:

$$\mathbf{d}(t) = c\mathbf{A}\mathbf{i}_{tm}(t), \tag{3.7}$$

where, $\mathbf{d}$ gives the electrogram data vector generated using this method. It contains the electrogram measurements captured at the N_e electrodes. The scalar c denotes the constants given by: $c = \frac{a}{4\pi\sigma_e}$. The transmembrane current is given by the vector $\mathbf{i}_{tm}$. Matrix $\mathbf{A}$ is the N_e x N matrix containing the inverse distances of each electrode to each voxel within the imaging domain $\mathbb{D}_{im}$. The matrix $\mathbf{A}$ can be written as:

$$\mathbf{A} = \begin{bmatrix} \frac{1}{||\mathbf{x}_1 - \mathbf{x}'_1||} & \frac{1}{||\mathbf{x}_1 - \mathbf{x}'_2||} & .... & \frac{1}{||\mathbf{x}_1 - \mathbf{x}'_N||} \\ \frac{1}{||\mathbf{x}_2 - \mathbf{x}'_1||} & \frac{1}{||\mathbf{x}_2 - \mathbf{x}'_2||} & .... & \frac{1}{||\mathbf{x}_2 - \mathbf{x}'_N||} \\ : & : & .... & : \\ : & : & .... & : \\ \frac{1}{||\mathbf{x}_{Ne} - \mathbf{x}'_1||} & \frac{1}{||\mathbf{x}_{Ne} - \mathbf{x}'_2||} & .... & \frac{1}{||\mathbf{x}_{Ne} - \mathbf{x}'_N||} \end{bmatrix}. \tag{3.8}$$

Equation (3.7) gives the forward model for data generation. This equation relates the transmembrane current distribution to the recorded electrogram signals. When the transmembrane current vector is known, the electrogram measurement data at individual electrodes can be determined by applying the matrix $\mathbf{A}$, that contains the inverse distances, to the current vector $\mathbf{i}_{tm}$. The recorded electrogram value thus depends on the position of the electrode with respect to every point within the volume domain and the transmembrane current values at each point within the volume domain.

3.2 Simulation Setup

In this section, the simulation setup used for estimating the location of atrial activity is introduced. A region of the heart is modelled as a clearly defined volume domain. Firstly, the generation of a transmembrane current grid that represents the atrial activity present within this volume is explained. Secondly, the setup of the volume domain along with the placement and orientation of the electrode array used for the measurement is discussed. The simulation setup explained is considered to be a baseline setup for the imaging procedure to locate the region where atrial activity is prominent. Several modifications are made to this simulation setup in Chapter 4 to analyse the changes in the resulting images when variations in the location of the current grid within the volume domain are introduced.

3.2.1 Generation of transmembrane current grids

The generation of transmembrane current grids used in this research is derived from [33] and [34]. An electrogram is the record of changes in the potentials of many cells surrounding the

electrode. These changes in cellular potentials are the result of action potential propagation in the tissue. This propagation in a two-dimensional (2D) tissue can be modeled using the following reaction-diffusion equation: [35]

$$C\frac{\partial V(x,y,t)}{\partial t} = I(x,y,t) + I_{st}(x,y,t) - I_{ion}(x,y,t,V), \tag{3.9}$$

where $V(x,y,t)$ is the extracellular potential at a location given by (x,y) at time t. The total transmembrane capacitance is given by $C = 1\,\mu\text{Fcm}^{-2}$, $I_{st}(x,y,t)$ is the stimulus current and $I_{ion}(x,y,t,V)$ denotes the total ionic current computed using the Courtemanche model [25].

For the generation of a transmembrane current grid, a 2D grid of dimensions 101x83, consisting of heterogeneous tissue with zones of reduced and no conductivity is simulated. Figure 3.2(a) shows the normalized conductivity map for the simulated tissue grid. A stimulating current is injected at the bottom right of the tissue grid for 1 ms as indicated in the activation map in Figure 3.2(b). Each pixel in the activation map corresponds to the local activation time (LAT) of a cell which essentially indicates the time when the cell potential reaches a threshold value of -40mV in the depolarization phase of the AP [26].

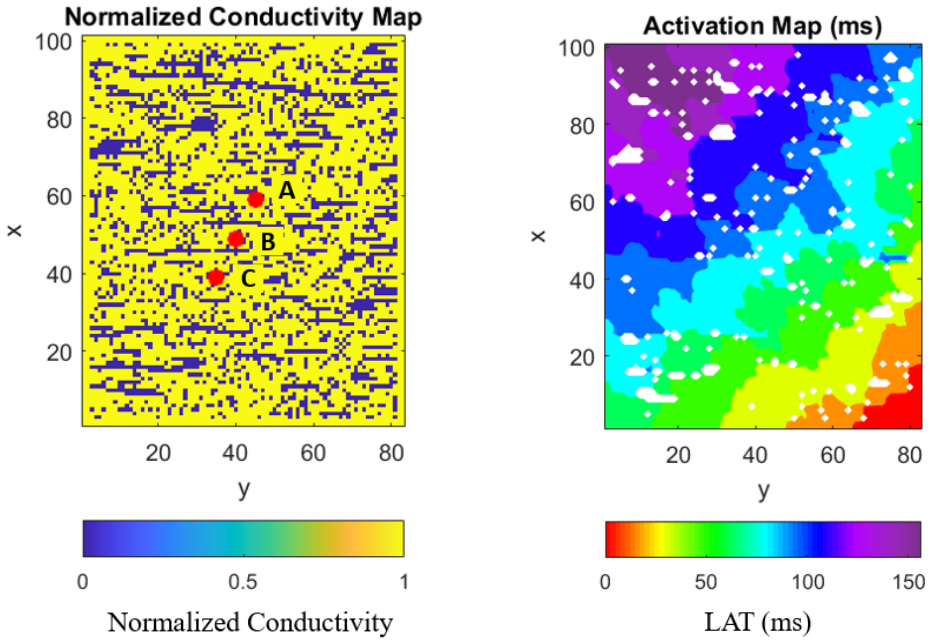

(a) (b)

Figure 3.2: (a) The normalized conductivity map for the heterogeneous tissue with zones of reduced and no conduction. (b) The corresponding activation map.

Figure 3.3 also shows the three resulting electrograms recorded at different electrode positions indicated by A,B,C on the conductivity map in Figure 3.2(a).

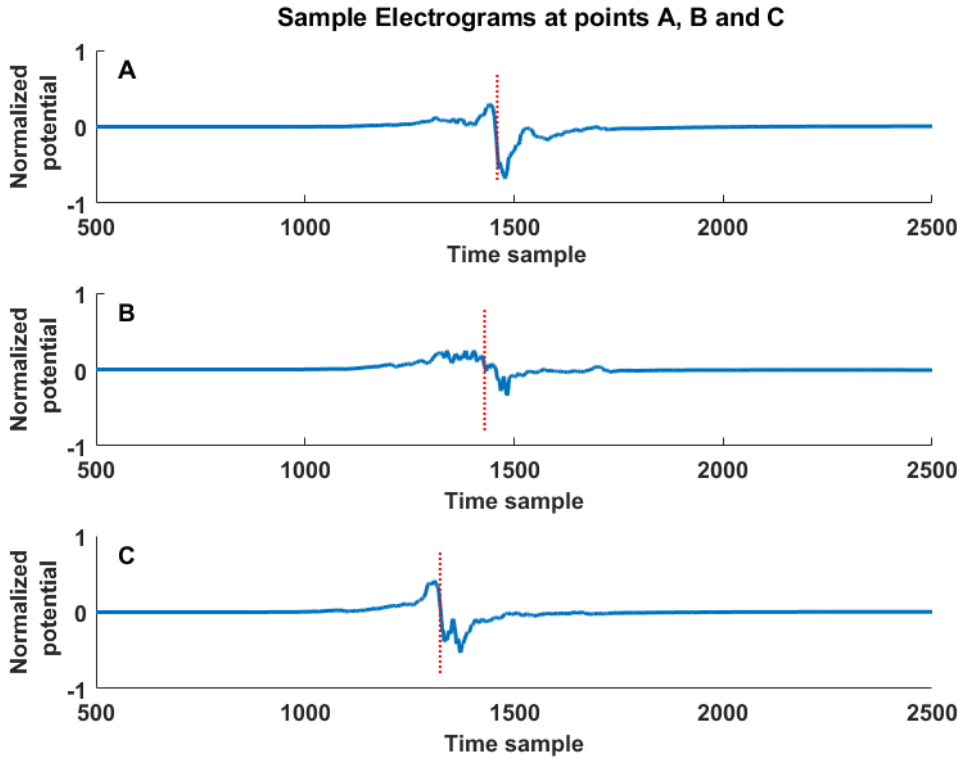

Figure 3.3: Three example electrograms recorded by electrodes at positions A, B and C indicated by the red dots in the normalized conductivity map of the simulated tissue grid in Figure 3.2 (a)

The total simulation time considered is 600 ms. The sampling time for EGM recording by electrodes is taken to be 0.1 ms. Out of the 6000 generated samples, a subsection of 1101 samples where atrial activity is observed is considered for this study. It is assumed that these samples have been preprocessed to get rid of the ventricular activity and that the ventricular interference in these samples is negligible. The transmembrane current at location $\mathbf{x}'$ and time t is given as:

$$I_{tm}(\mathbf{x}', t) = S_\nu^{-1} \nabla \cdot \mathbf{\Sigma}(\mathbf{x}') \nabla V(\mathbf{x}', t), \tag{3.10}$$

where $S_\nu^{-1} \simeq 0.24\,\mu\text{m}^{-1}$ is the cellular surface to volume ratio, $\mathbf{\Sigma}(\mathbf{x}')$ is the intracellular conductivity tensor and $V(\mathbf{x}', t)$ is the extracellular potential recorded at $\mathbf{x}'$ at time t [26]. The transmembrane current values generated for a central sub-grid of 43x25 cells is taken into account for the simulation setup used for volume imaging in this thesis.

3.2.2 Simulation setup for Volume Imaging

For location estimation of atrial activity, a volume domain $\mathbb{D}_{im}$ consisting of 123x100x10 non-overlapping voxels is considered. This represents the spatial extent of the imaging

domain. The transmembrane current generated in Section 3.2.1 exists as a two-dimensional grid at a certain depth within the imaging volume. The current grid has a dimension of 43x25 cells with an inter-cell distance of $\Delta x = 0.6$ mm. Each element of the current grid represents the transmembrane current value at the specific location within the volume domain. In this simulation, a two-dimensional electrode array of dimensions 15x9 is used. The inter-electrode distance considered is 3 $\Delta x = 1.8$ mm. This covers the entire recording area for the current grid. The electrode array is placed on the $z = 0$ plane in such a way that the bottom left corner of the array coincides with the origin of the coordinate system for the considered volume domain.

Figure 3.4 shows a representation of the simulation setup used for the volume imaging. The yellow grid within the shaded blue volume domain represents the 43x25 current grid whose location is to be determined. The 15x9 electrode array is indicated by the red grid and exists on the $z = 0$ plane. It is important to note that the setup consists of 123000 voxels, a 43x25 grid of cells with transmembrane current values indicating the irregular atrial activity and 135 electrodes that record the electrogram measurements.

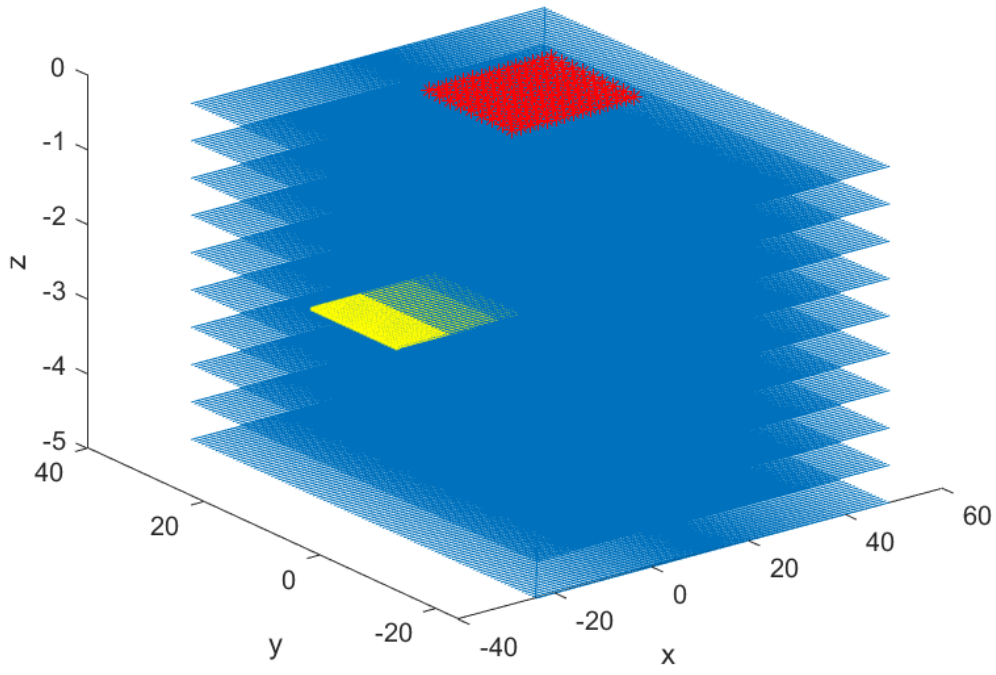

Figure 3.4: Simulation setup for volume imaging. The domain $\mathbb{D}_{im}$ used for imaging is indicated in blue. The yellow 2-D grid at a certain depth indicates the current grid of 43x25 cells and the 15x9 electrode array on the surface ($z = 0$ plane) is indicated by the red grid.

Imaging for Location Estimation of Atrial Activity

4

Locating the atrial activity in a given volume domain can be valuable information for guided ablation procedures undertaken to precisely target and eliminate AF triggers. In this chapter, a simple but effective and fast imaging method is explored to primarily locate the region where the irregular atrial activity is prominent within a chosen volume domain in the heart. The volume domain is assumed to consist of homogeneous cardiac cells with identical dimensions and a constant extracellular conductivity. The analysis is carried out in the frequency domain and the effect of frequency variations on the current grid is also taken into account. The inverse problem of reconstructing the three-dimensional transmembrane current distribution within the volume domain is solved. The key focus in this chapter is on the generation of backprojection images and the information that can be extracted from these images for estimating the location and depth where the atrial activity is prominent within the volume.

4.1 Frequency domain Imaging

4.1.1 Data generation

The electrogram data is generated based on the matrix multiplication model as denoted in Eq. (3.7). A frequency domain representation of the data is generated by applying the Fourier Transform, which is given as

$$\mathbf{d}(\omega) = c\mathbf{A}\mathbf{i}_{tm}(\omega). \tag{4.1}$$

The frequency domain representation gives an insight into the frequency specific components in the electrogram data. Since we consider a large imaging domain with 123000 voxels and the number of electrodes used for measurement is just 135, we have an underdetermined system. Given the electrogram data $\mathbf{d}$ recorded by the 135 electrodes placed on the $z = 0$ plane, we aim to solve the inverse problem of reconstructing the current distribution by exploiting the spatial information available in the matrix $\mathbf{A}$.

4.1.2 Generation of Backprojection image

Generating a backprojection image from electrogram data can aid in locating the atrial activity in a volume domain by providing a spatial representation of the electrical activity distribution in the atria. Backprojection is a method for reconstructing a spatial map from recorded data that is extensively used in imaging and signal processing. In the broader

setting of atrial activity localization, backprojection imaging can be used to identify the regions in the atria that are actively involved in irregular electrical activity.

Solving the inverse problem involves the reconstruction of the underlying electrical sources based on the recorded electrogram measurements and the geometry and position of the electrode array. Matrix $\mathbf{A}$ in Eq.(4.1) contains the inverse distances from each electrode in the electrode array to each voxel within the imaging domain $\mathbb{D}_{im}$. The matrix $\mathbf{A}$ thus contains information about the geometry and location of the electrode array with respect to the considered volume domain.

The electrogram measurement data $\mathbf{d}(\omega)$ obtained from Eq.(4.1) is used to generate a backprojection image of the source onto the imaging domain. For the considered underdetermined system where $\mathbf{A}$ is full rank, the minimum norm solution is given as

$$\mathbf{i}_{mn}(\omega) = \mathbf{A}^T(\mathbf{A}\mathbf{A}^T)^{-1}\mathbf{d}(\omega). \tag{4.2}$$

Since $\mathbf{A}$ is a very wide matrix, the computation of the inverse is often not feasible. If we ignore the action of the inverse, the transpose of the inverse distances matrix $\mathbf{A}$ acts as a backprojection operator, giving the backprojection image, often referred to as the dirty image in astronomy. The backprojection image is obtained as,

$$\mathbf{i}_{im}(\omega) = \mathbf{A}^T\mathbf{d}(\omega). \tag{4.3}$$

Using the measured data $\mathbf{d}(\omega)$, we attempt to reconstruct the source or electrical activity distribution within the volume that could have resulted in the measured data that was recorded at the electrode array. To analyse the generation of backprojection images at different frequencies, a simulation setup shown in Figure 4.1 (a) is introduced where the current grid is located to the right of the electrode array, with an overlap of 3.6 mm with the electrode array. The current distribution in the volume is reconstructed for the electrogram data at three different frequencies. For each of the three-dimensional reconstructions, a y-slice of the volume running through the centre of the electrode array at $y = 7.2$ mm is extracted to be imaged. Figure 4.1 (b) shows a schematic representation of the y-slice indicated in black being extracted from the volume. The y-slice is extracted in an attempt to locate the electrical activity along the x-direction and to get an estimate of the depth at which the current grid is present within the volume.

Figure 4.2 gives the three backprojection images generated by considering the electrogram data at three different frequencies. The frequencies are chosen such that they cover a range of frequencies from lower, middle and high frequencies. The generated images give an indication of the location of the current grid or the region of electrical activity along the x-direction. In the backprojection images, it is observed that the peaks or prominent areas of electrical activity are concentrated at the depth where the electrode array is located ($z = 0$ plane) and the intensity of the peak decreases as the depth increases. This is due to the attenuation of the image as it propagates further within the cardiac tissue. This makes it difficult to get an estimate of the depth at which the atrial activity is occurring through this imaging method.

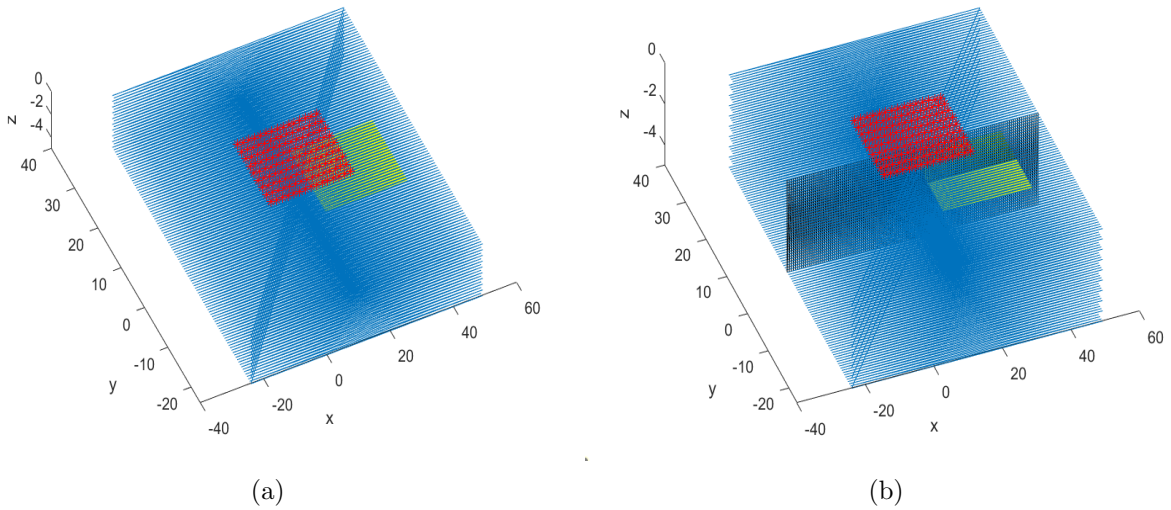

Figure 4.1: (a) The simulation setup considered for generating backprojection images at different frequencies (b) Representation of the y-slice at $y = 7.2$ mm that is extracted for imaging.

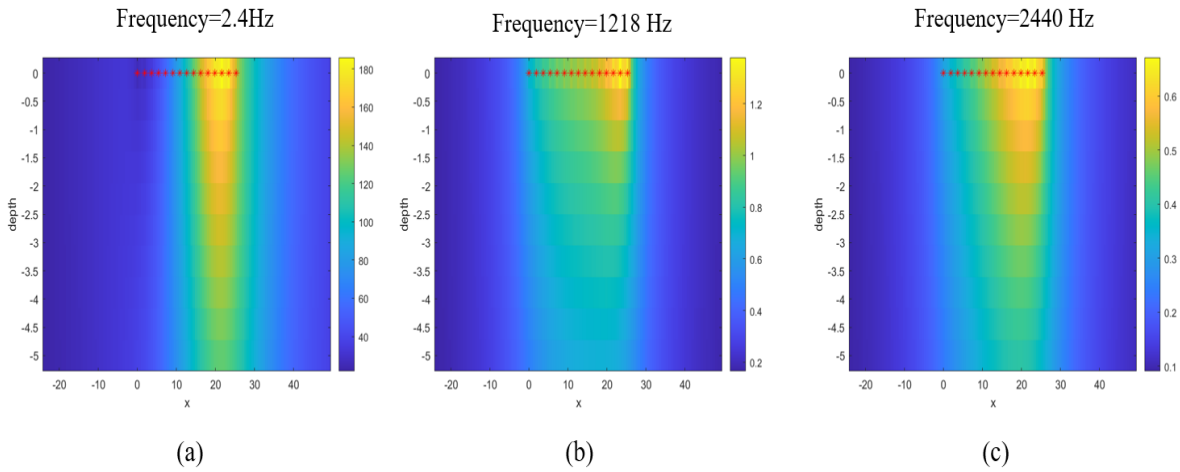

Figure 4.2: Backprojection images generated using electrogram data at three different frequencies

The observed backprojection images in Figure 4.2 indicate a narrow and more distinct peak at lower frequencies. When the data at higher frequency is considered, an increased distortion and blurring of the peak is observed, making it difficult to accurately estimate the potential source location.

In order to further identify any dependencies that the current exhibits on the frequency being considered during the imaging procedure, the spatial distribution of current in the 43x25 current grid at different frequencies is analysed. The same three frequencies are taken into account and the spatial plot of the transmembrane current at these three different frequencies are shown in Figure 4.3. It is observed that the current distribution over space is random and does not follow a specific pattern that varies with varying frequency. A larger intensity of current contribution exists at low frequencies and the contribution is considerably reduced as the frequency increases.

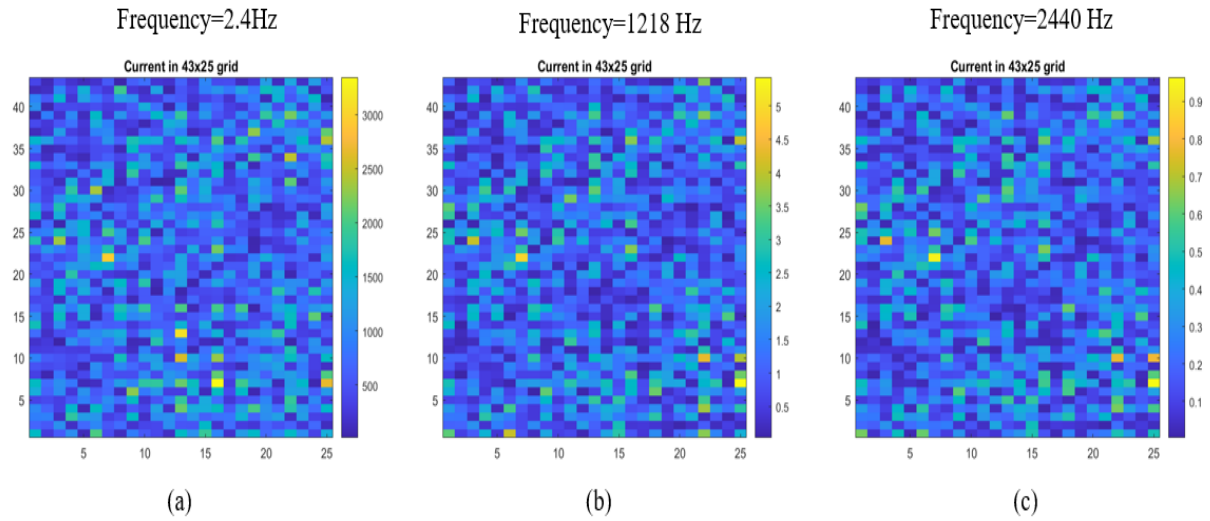

Figure 4.3: The spatial distribution of current in the 43x25 grid at different frequencies

In the next section, we assume equal contributions of data recorded at different frequencies for the generation of the backprojection image and introduce the so-called frequency-independent current case and analyse the results obtained for this case. We assume frequency independence of the current to reduce the effect of frequency dependent variations and improve the accuracy of localization of the peak in the backprojection images. A comparison is drawn for the resulting backprojection images obtained in both cases where the current is frequency dependent and frequency independent. However, it is to be noted that the proposed frequency-independent model may not completely capture the true behavior of the electrical activity or current distribution in all scenarios.

4.1.3 Frequency-independent Current

In this section, we assume the transmembrane current $\mathbf{i}_{tm}$ to be frequency independent. For the generation of the recorded electrogram data vector, Eq. (4.1) can be re-written as:

$$\mathbf{d}(\omega) = \mathbf{A}\mathbf{i}_{tm}. \tag{4.4}$$

The data at F different frequencies $\omega_1, \omega_2, ...\omega_F$ is given as:

$$\begin{bmatrix} \mathbf{d}(\omega_1) \\ \\ \mathbf{d}(\omega_2) \\ \\ : \\ : \\ \mathbf{d}(\omega_F) \end{bmatrix} = \begin{bmatrix} \mathbf{A} \\ \\ \mathbf{A} \\ \\ : \\ : \\ \mathbf{A} \end{bmatrix} \mathbf{i}_{tm}. \tag{4.5}$$

By considering equal contributions of the data recorded at F frequencies weighted by the inverse distances matrix $\mathbf{A}$, the reconstructed transmembrane current can be written as,

$$\mathbf{i}_{im} = \sum_{f=1}^{F} \mathbf{A}^T \mathbf{d}(\omega_f). \tag{4.6}$$

By applying this new backprojection operator, the reconstructed current distribution equation in a matrix multiplication form is given as:

$$\mathbf{i}_{im} = \mathbf{B}^T \mathbf{d}', \tag{4.7}$$

where,

$$\mathbf{B} = \begin{bmatrix} \mathbf{A} \\ \\ \mathbf{A} \\ \\ : \\ : \\ \mathbf{A} \end{bmatrix} \quad \text{and} \quad \mathbf{d}' = \begin{bmatrix} \mathbf{d}(\omega_1) \\ \\ \mathbf{d}(\omega_2) \\ \\ : \\ : \\ \mathbf{d}(\omega_F) \end{bmatrix}. \tag{4.8}$$

Matrix $\mathbf{B}$ is formed by stacking the $\mathbf{A}$ matrix vertically F times. $\mathbf{A}$ is the inverse distances matrix that defines the distances from the individual electrodes in the electrode array to the voxels within the volume domain. The vector $\mathbf{d}'$ now contains the measured data at F different frequencies given by $\mathbf{d}(\omega_1), \mathbf{d}(\omega_2), ...\mathbf{d}(\omega_F)$.

To obtain the backprojection images in this case (assuming current to be frequency independent), the baseline simulation setup explained in Section 3.2.2 is used. Here, F is assumed to be 3. Hence, the data values at 3 frequencies are considered to form the $\mathbf{d}'$ vector. The same three frequency values as in the previous section ranging over low, middle and high frequencies are considered. Matrix $\mathbf{B}$ is then taken to be matrix $\mathbf{A}$ stacked vertically 3 times. An experiment is carried out where the location of the current grid within the volume domain is varied along the x-axis to analyse how the displacement of the current grid is reflected in the backprojection image that is generated.

Initially, the current grid is assumed to be at the left in the volume domain while the electrode array is at the centre as denoted in Figure 4.4 (a) by the red *. Figure 4.4 (b) shows the backprojection image formed by using Eq. (4.7). A y-slice of the volume running through the centre of the electrode array at $y = 7.2$ mm is selected to be imaged.

The backprojection image indicates the location of the current grid within the volume domain and gives an estimate of the x-coordinate information of where the atrial activity occurs within the volume domain. This information is valuable in localizing the abnormal or irregular atrial activity. Identifying specific regions of abnormal activity can guide the placement of catheters for targeted ablation, thus increasing the accuracy and effectiveness of the procedure.

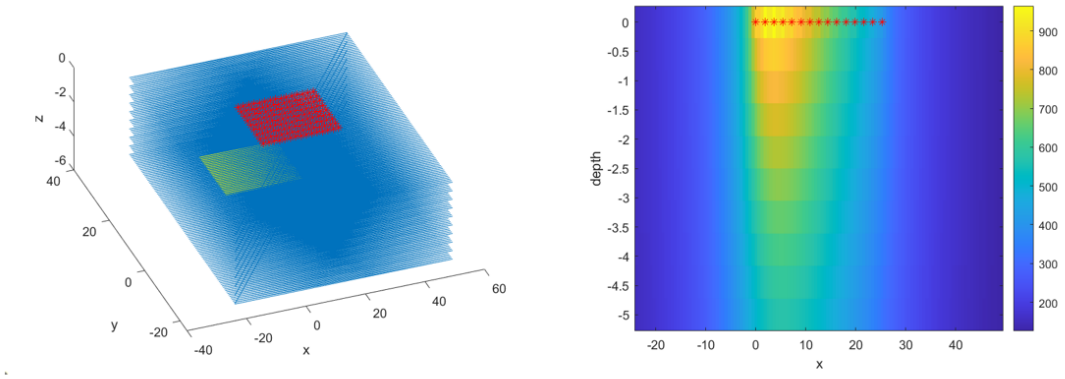

Figure 4.4: (a) Sample case where the current grid is towards the left of the electrode array used for measurement. (b) The backprojection image generated.

On modifying the setup and moving the current grid towards the right, the change is reflected in the backprojection image with respect to the electrode position as shown by the red *. Figure 4.5 (a) shows the sample case when the current grid is centrally located with respect to the electrode array, at a distance of 17.4 mm from its initial position. Figure 4.6 (a) shows the case when the current grid is placed at distance of 48 mm to the right of its initial position. The backprojection images seen in Figure 4.5 (b) and Figure 4.6 (b) give an indication of the modified position of the current grid within the volume domain.

The backprojection image in the frequency independent case emphasizes the regions where the transmembrane current is concentrated, showing atrial activity. Higher values in the backprojection image indicate regions with higher electrical activity. The peak has less blurring and is more concentrated at the location of the current grid as compared to the images obtained for the frequency dependent current case, especially for the middle and high frequencies. In the backprojection images generated in the frequency-independent case too, the peak of the current distribution is found to be concentrated at the depth where the electrode array is located ($z = 0$ plane) and gradually fades with increasing depth. Therefore, using this imaging method, we are unable to determine the depth at which the atrial activity is prominent from the recorded electrogram measurements.

The backprojection image, however, gives a visual estimate of the location along the

x-axis where the atrial activity occurs within the volume domain considered. The known position of the electrode acts as a reference. The exact x-coordinate information can be extracted to obtain an estimate of where the atrial activity begins in the x-direction. This can be utilised to perform localized analysis of the tissue in this region and accordingly guide catheter placement in ablation procedures. This is a straightforward imaging method that is not computationally complex and can be considered as a first step in estimating the location of the atrial activity within a volume domain. The simple imaging method is also computationally fast. The MATLAB code uses for loops and takes 40.317 seconds to run on a PC with an i7 core processor.

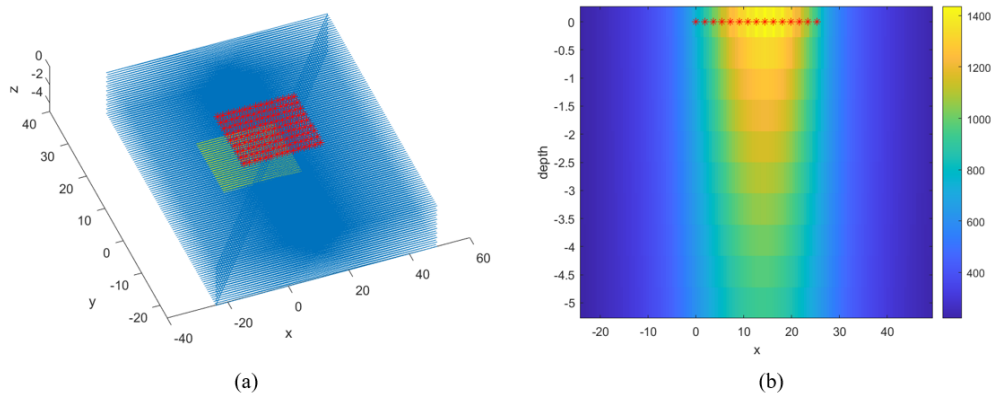

Figure 4.5: (a) Sample case where the current grid is centrally located with respect to the electrode array used for measurement. (b) The backprojection image generated.

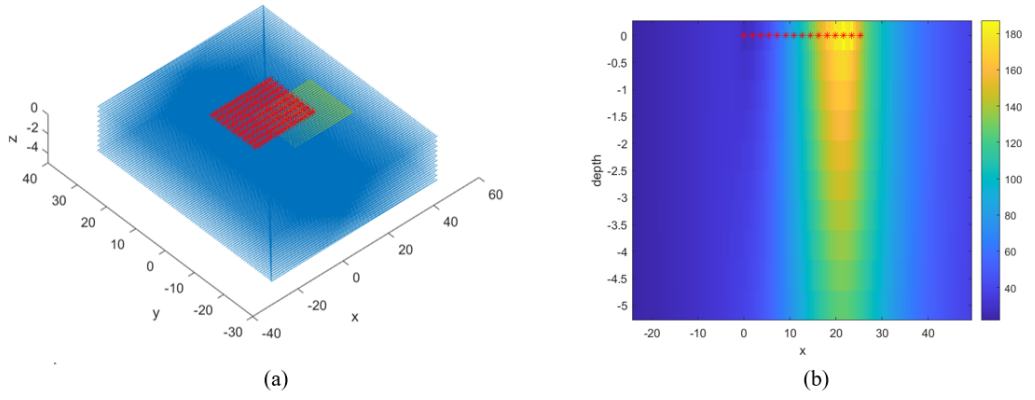

Figure 4.6: (a) Sample case where the current grid is displaced towards the right of the electrode array used for measurement. (b) The backprojection image generated.

The y-coordinate information of the region with irregular atrial activity within a volume domain can be obtained in a similar manner by imaging an x-slice of the reconstructed transmembrane current distribution volume. Figure 4.7 (a) shows a centrally located current grid with respect to the electrode array along the y-axis. An x-slice of the reconstructed transmembrane current volume running through the electrode array at $x = 11.4$ mm is chosen to be imaged. The generated backprojection image for this setup is shown in Figure 4.7 (b). The image shows the distribution of the atrial activity along the y-axis with respect to the electrode array denoted by the red *.

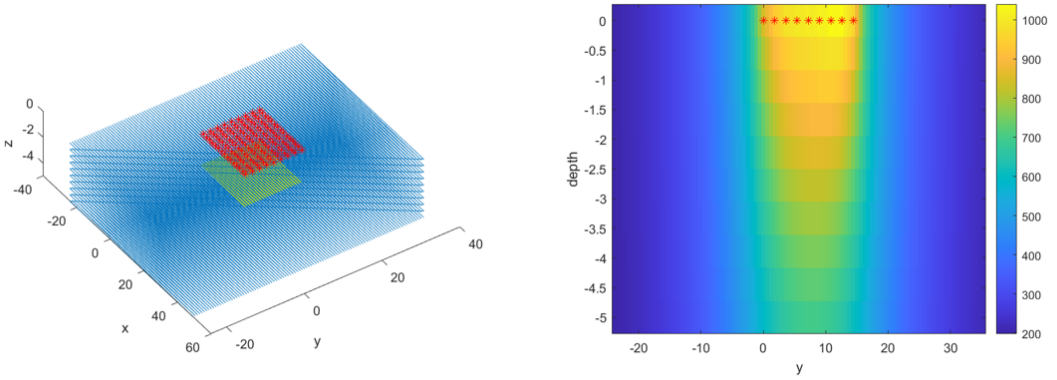

(a) (b)

Figure 4.7: (a) The current grid is centrally located with respect to the electrode array used for measurement. (b) The backprojection image generated with depth vs y information.

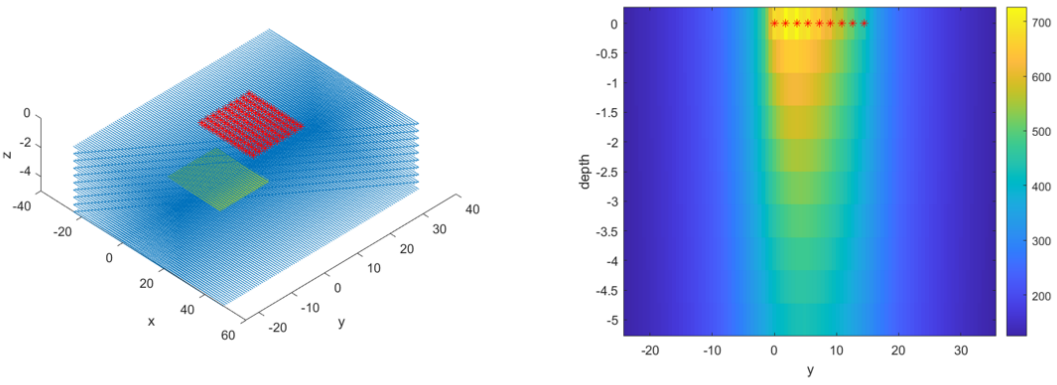

(a) (b)

Figure 4.8: (a) Sample case where the current grid is displaced towards the left of the electrode array used for measurement. (b) The backprojection image generated with depth vs y information.

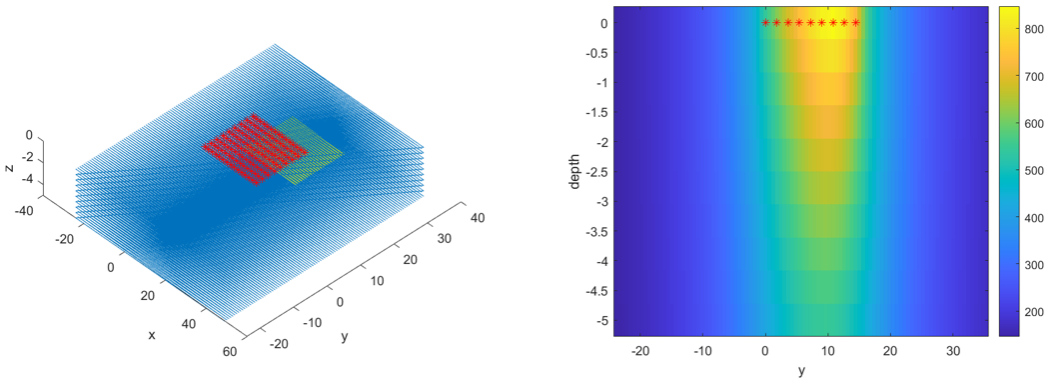

(a) (b)

Figure 4.9: (a) Sample case where the current grid is displaced towards the right of the electrode array. (b) The backprojection image generated with depth vs y information.

In Figure 4.8 (a), the setup is modified in such a way that the current grid is displaced to the left by 12 mm and is on the left of the electrode array. This displacement is reflected in the backprojection image generated in Figure 4.8 (b). Similarly, Figure 4.9 (a) has a modified setup where the grid is displaced towards the right by 12 mm and is on the right of the electrode array. The backprojection image with respect to depth vs y generated in Figure 4.9 (b) gives a visual estimate of the y-coordinate information in this setup. In the above images generated to obtain an estimate of the y-coordinate information, it is again observed that the peak in the image is concentrated at the depth where the electrode array is placed at the $z = 0$ plane. This limitation is consistent with the one seen in the backprojection images that indicate the depth vs x information. The depth estimate of the current grid from the surface cannot be extracted from these images.

In the following section, the backprojection images are analysed to study the spatial resolution when there are multiple sites of irregular atrial activity within the volume. The analysis in the following section makes use of the backprojection images formed by taking a y-slice of the reconstructed transmembrane current distribution. These images give the depth vs x information. It is to be noted that in all these cases, similar results can be reproduced for the y-coordinate information by imaging an x-slice of the reconstructed transmembrane current distribution that gives the depth vs y information.

4.2 Analysis of Spatial resolution for two current grids present within the volume domain

Atrial Fibrillation is characterised by the irregular beating of the heart. During AF, electrical impulses may be triggered at many locations within the atria, leading them to contract

in an unorganized manner. In order to identify the presence of the irregular atrial activity occurring at different locations within a volume domain, a new experimental setup with two identical current grids of 43x25 cells placed in the volume domain is now introduced. In this section, we analyse the spatial resolution or the ability of the generated backprojection image to distinguish between atrial activity happening at two different regions within the volume domain.

The baseline simulation setup from Section 3.2.2 is modified to include another 43x25 current grid at different locations within the volume domain. To simplify the analysis, one current grid (Grid 1) is fixed at a position with 50% overlap with the electrode array on its left half. The electrode array occupies a length of 25.2 mm along the x-direction. Hence, the grid covers 12.6 mm of the electrode array. The right grid (Grid 2) is also initially placed with a 50% overlap with the electrode array. Figure 4.10(a) shows the top view of the arrangement of the current grids in the volume domain. The electrode array is indicated by the red *. The three-dimensional current distribution is generated by applying the backprojection operator as in Eq. (4.7). The y-slice running through the centre of the electrode array at $y = 7.2$ mm is extracted and imaged. The resulting backprojection image in terms of depth vs x shown in Figure 4.10(b) has a blurred indication of the region of the atrial activity location. The grids are not separated spatially in this image and there are no individual peaks that can be visually distinguished.

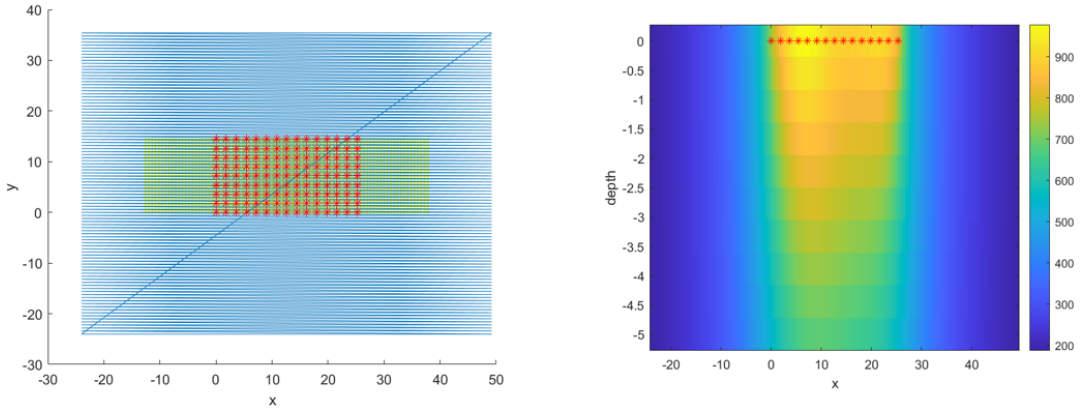

Figure 4.10: (a) **Case 1**: The arrangement with two grids each placed at 50% overlap with the electrode array. (b) The backprojection image generated.

In the setups shown in Figure 4.11, Grid 2 is displaced such that its overlap with the electrode array is decreased in steps of the inter-electrode distance of 1.8 mm and it is moved in the positive x-direction, away from Grid 1. Grid 1 is fixed at the 50% overlap position. Figure 4.11 (a) and (b) show the arrangement where the distance between the current grids is 2 times the inter-electrode distance and the resulting backprojection image respectively. The resulting image is now such that two separate peaks can be distinguished

and the left peak is more prominent since Grid 1 has a larger overlap with the electrode array. Figure 4.11 (c) shows the arrangement where Grid 2 is moved further in the positive x-direction such that the grids are at a distance of 3 times the inter-electrode distance. The backprojection image obtained in this case in Figure 4.11 (d) gives two peaks that are completely spatially resolved indicating the different regions of atrial activity along the x-axis. This information can be valuable in estimating the location of two closely spaced regions within the atria that are potentially AF trigger sites.

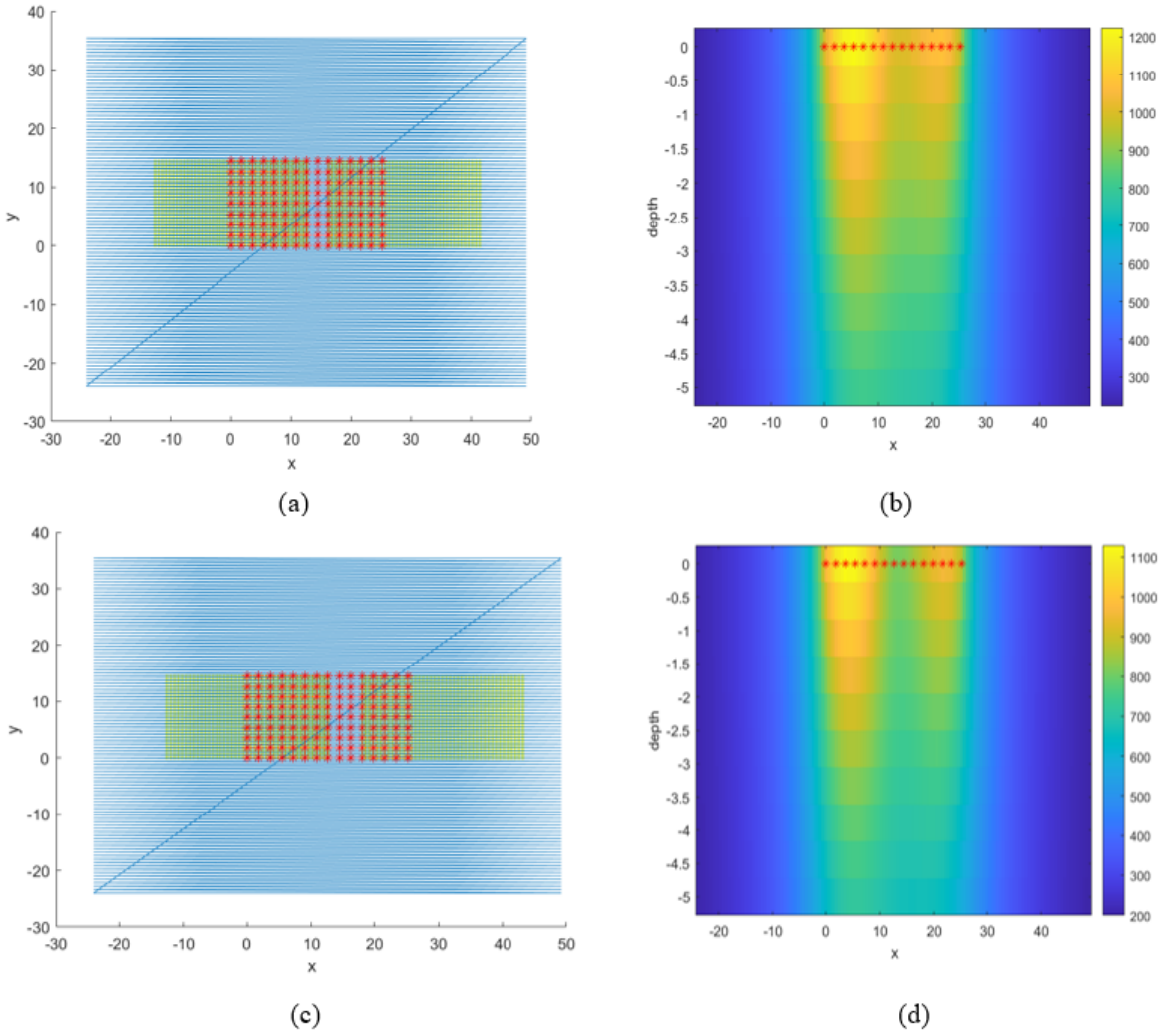

Figure 4.11: (a) **Case 2**: Two current grids placed at a separation of 2*1.8 mm. (b) The backprojection image generated in Case 2. (c) **Case 3**: Two current grids placed at a separation of 3*1.8 mm. (d) The backprojection image generated in Case 3.

4.3 Depth estimation

The previously discussed simulations and resulting backprojection images provided an estimate of the x and y-coordinate information for the location of the irregular atrial activity using the epicardial electrogram measurements as a basis for reconstructing the transmembrane current distribution. However, a limitation of the proposed method was that the depth of the atrial activity with respect to the electrode array used for the measurement could not be determined. The peak or high intensity areas in the generated backprojection images were concentrated at the $z = 0$ plane where the electrode array was placed for measuring the epicardial electrograms. This restricted the output to the estimates for the location of the current grid along the x and y axes only. In this section, a different placement and orientation of the electrode array is considered that would provide an estimate of the depth at which the irregular atrial activity is prominent.

In the previous simulation setups used for the location estimate, the electrode array used to capture the electrogram measurements was placed on the surface of the volume of cardiac tissue thus acquiring the epicardial electrogram readings. In a clinical setting, the epicardial electrogram readings are obtained using a high resolution electrode during open-heart surgery. However, electrogram readings can be acquired at specific tissue locations with the use of electrodes attached to a catheter that is inserted into the heart. The manipulation of the mapping catheter gives rise to intracardiac electrogram measurements that assist in the 3-D reconstruction of the regions of interest [36],[37]. The use of a fully-elastic electrode array to capture real-time electrophysiological mapping of AF in vivo is presented in [38]. For the depth estimation process, the simulation setup discussed in Section 3.2.2 is modified to include an electrode array that is placed within the volume.

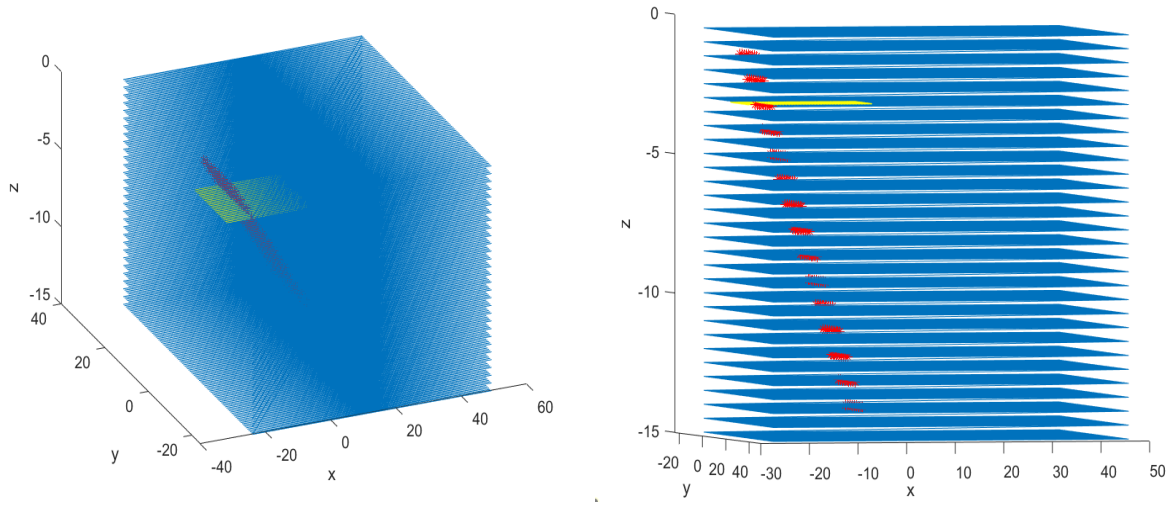

(a) (b)

Figure 4.12: Simulation setup for depth estimation

Figure 4.12 shows the simulation setup employed for depth estimation. A larger domain in terms of depth is considered to allow experimentation with distinct depth values. The volume domain in this setup has been subdivided into 123x100x30 voxels. The depth values range from 0 mm to a depth of 15mm below the epicardial surface. The same electrode array of 15x9 electrodes is used to capture the electrogram readings. The electrode array is placed at an angle of 68° with the x-axis. The angle is chosen such that the electrode array covers the maximum depth and a larger volume for depth measurement compared to an electrode array placed vertically within the domain.

The simulation setup in Figure 4.12 is modified in such a way that the depth of the current grid is varied. The transmembrane current distribution is reconstructed using the method highlighted in Section 4.1.3 considering the different positions of the electrodes in this setup. A y-slice of the reconstructed distribution through the centre of the electrode array at $y = 0$ mm is extracted to be imaged. The backprojection images are generated for different depth values of the current grid in the simulation setup.

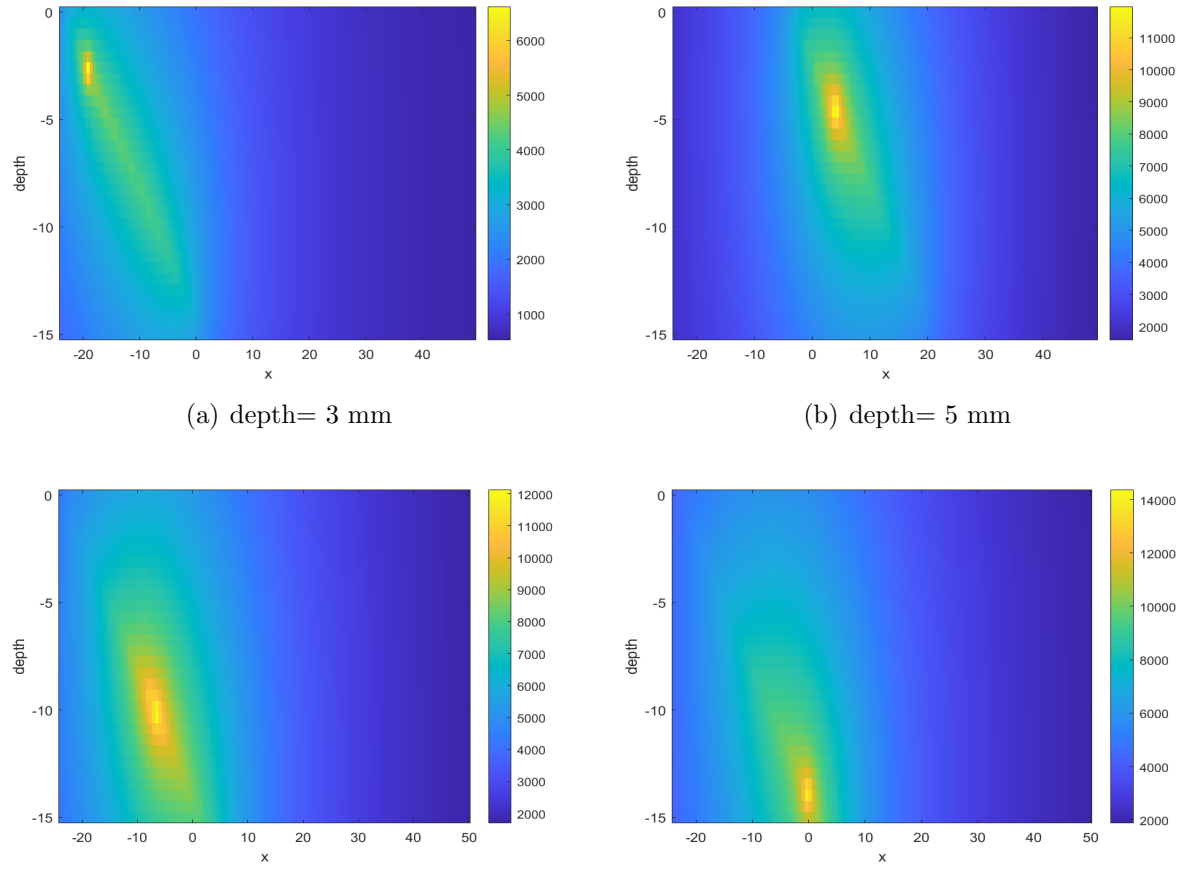

(a) depth= 3 mm

(b) depth= 5 mm

(c) depth= 10 mm

(d) depth= 14 mm

Figure 4.13: Backprojection images generated using the modified simulation setup for different depths of the current grid

Figure 4.13 shows the backprojection images obtained for four depth values of the current grid at 3 mm, 5 mm, 10 mm and 14 mm below the surface. A blurred peak of high intensity values is observed around the expected depth of the current grid in the generated backprojection images, thus giving an estimate of the depth at which the irregular electrical activity is prominent. The x and y-coordinate information obtained from the epicardial electrogram readings can be utilised to accurately place the electrode array for depth measurement. The depth at which the peak is observed can be extracted to determine the depth to which the catheter must be inserted to ablate the diseased tissue. Combining the location estimate of the current grid along the x and y axes with the depth estimate obtained using this method gives a more complete understanding of the region of irregular atrial activity within the considered volume domain.

It is to be noted that the technique presented above for depth estimation is not refined enough to be applied in a clinical setting in its current form. The electrode array placement within the volume of heart tissue is an intra-operative and highly invasive procedure and would require consultation with medical experts to determine its feasibility. However, the proposed method offers a promising path for future investigations into targeted ablation for the treatment of AF.

In the following chapter, a Singular Value Decomposition (SVD) of the inverse distances matrix is considered to study its effect on the reconstruction of the transmembrane current distribution, the backprojection images and the accuracy of localization of the irregular atrial activity in the generated images.

5 Singular Value Decomposition

In this chapter, we use Singular Value Decomposition (SVD) of the inverse distances matrix to improve the accuracy of localization of the region with irregular atrial activity while ensuring that the method used for imaging is still computationally fast. A comparison is drawn between the visual estimates of the depth vs x information obtained using this method and the backprojection images generated in Chapter 4.

5.1 Reconstruction of transmembrane current using SVD

For the frequency-dependent current case discussed in Section 4.1.2 , the forward model for data generation was given as:

$$\mathbf{d} = c\mathbf{A}\mathbf{i}_{tm}. \tag{5.1}$$

The electrogram measurement data $\mathbf{d}$ was generated by applying the inverse distances matrix $\mathbf{A}$ to the transmembrane current vector $\mathbf{i}_{tm}$. $\mathbf{A}$ is a full rank real matrix containing the inverse distances of the electrodes to the voxels. The number of electrodes considered are 15x9=135 and the total number of voxels is 123x100x10=123000 voxels. The system under consideration is an underdetermined system where the number of unknowns is larger than the number of measurements. For this system, the minimum norm solution is given by:

$$\mathbf{i}_{mn} = \mathbf{A}^T(\mathbf{A}\mathbf{A}^T)^{-1}\mathbf{d}. \tag{5.2}$$

The backprojection images of the reconstructed current distribution in Chapter 4 were obtained by ignoring the action of the inverse in Eq. (5.2). Since we obtain reduced blurring and better location estimates in the backprojection images generated for the frequency-independent current case discussed in the Section 4.1.3, we focus on this case for further analysis in this chapter. The electrogram data generation in this case is given by the equation:

$$\mathbf{d}' = c\mathbf{B}\mathbf{i}_{tm}. \tag{5.3}$$

The data $\mathbf{d}'$ is generated by applying the matrix $\mathbf{B}$ to the transmembrane current distribution vector $\mathbf{i}_{tm}$. The matrix $\mathbf{B}$ is formed by stacking the matrix $\mathbf{A}$ three times. The dimensions of matrix $\mathbf{A}$ are N_e x N. The number of electrodes N_e considered are 15x9=135 and the total number of voxels N is 123x100x10=123000 voxels. Hence, matrix $\mathbf{B}$ has the dimensions $3N_e$ x N (405 x 123000).

In order to simplify the notation in the following analysis, let the dimensions of $\mathbf{B}$ be given by m x n. $\mathbf{B}$ consists of real values and is a wide matrix since $m<n$.

The Singular Value Decomposition (SVD) of the $\mathbf{B}$ matrix can be given as

$$\mathbf{B} = \mathbf{U}\Sigma\mathbf{V}^T, \tag{5.4}$$

where, the matrix $\mathbf{U}$ =[$\mathbf{u}_1$.....$\mathbf{u}_m$] contains the left singular vectors, $\mathbf{V}$=[$\mathbf{v}_1$.....$\mathbf{v}_n$] contains the right singular vectors, and Σ is the diagonal matrix containing the non-negative singular values in descending order, written as,

$$\Sigma = \begin{bmatrix} \sigma_1 & 0 & \dots & 0 & 0 & \dots & 0 \\ 0 & \sigma_2 & \dots & 0 & 0 & \dots & 0 \\ \vdots & \vdots & \ddots & \vdots & \vdots & & \\ 0 & 0 & \dots & \sigma_m & 0 & \dots & 0 \end{bmatrix}. \tag{5.5}$$

Since the last $(n-m)$ singular values of $\mathbf{B}$ are zero, the last $(n-m)$ columns of $\mathbf{V}$ can be omitted to give the reduced SVD or "economy-size" SVD of $\mathbf{B}$:

$$\mathbf{B} = \hat{\mathbf{U}}\hat{\Sigma}\hat{\mathbf{V}}^T, \tag{5.6}$$

$$\hat{\Sigma} = \begin{bmatrix} \sigma_1 & 0 & \dots & 0 \\ 0 & \sigma_2 & \dots & 0 \\ \vdots & \vdots & \ddots & \vdots \\ 0 & 0 & \dots & \sigma_m \end{bmatrix}. \tag{5.7}$$

Matrix $\hat{\Sigma}$ is an m x m diagonal matrix, $\hat{\mathbf{U}}$ is a m x m orthogonal matrix ($\hat{\mathbf{U}}\hat{\mathbf{U}}^T = \mathbf{I}$), and $\hat{\mathbf{V}}^T$ is a wide matrix the same size as $\mathbf{B}$ (m x n). Matrix$\hat{\mathbf{V}}$ has orthonormal columns such that $\hat{\mathbf{V}}^T\hat{\mathbf{V}} = \mathbf{I}$.
The reconstructed current distribution $\tilde{\mathbf{i}}$ is now given by,

$$\tilde{\mathbf{i}} = \sum_{i=1}^{k} \frac{\mathbf{u}_i^T \mathbf{d}'}{\sigma_i} \mathbf{v}_i, \tag{5.8}$$

where, $\mathbf{u}_i$, $\mathbf{v}_i$ and σ_i denote the i^{th} left singular vector, i^{th} right singular vector and the i^{th} singular value respectively. k denotes the upper limit of singular values being considered to generate the three-dimensional current distribution.

Figure 5.1 shows a plot of the singular values of matrix $\mathbf{B}$. As discussed, matrix $\mathbf{B}$ has been generated by stacking matrix $\mathbf{A}$ three times. $\mathbf{A}$ is a full rank matrix and the rank ($\mathbf{A}$) = 135 that is equal to the number of electrodes considered for the electrogram measurement. A zoomed version of the singular value distribution of $\mathbf{B}$ is shown in Figure 5.2.

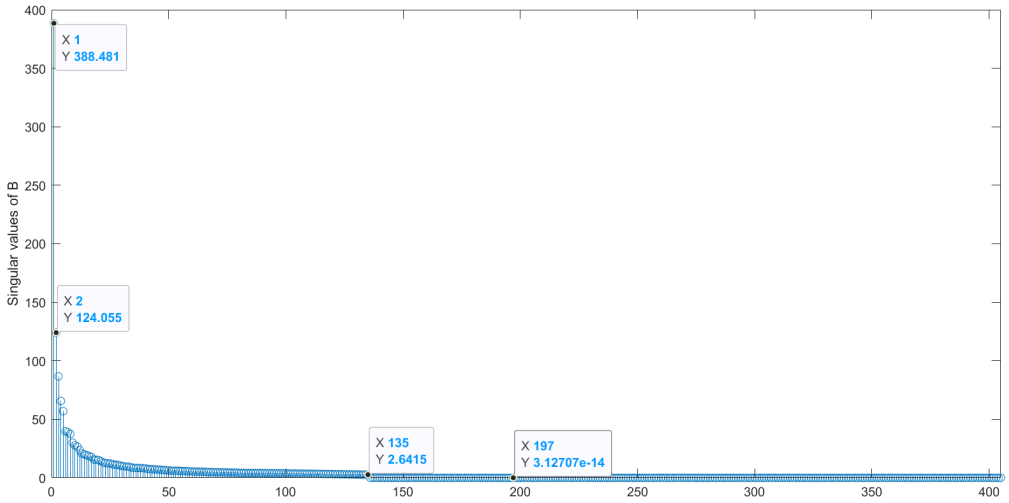

Figure 5.1: Singular values of matrix **B**

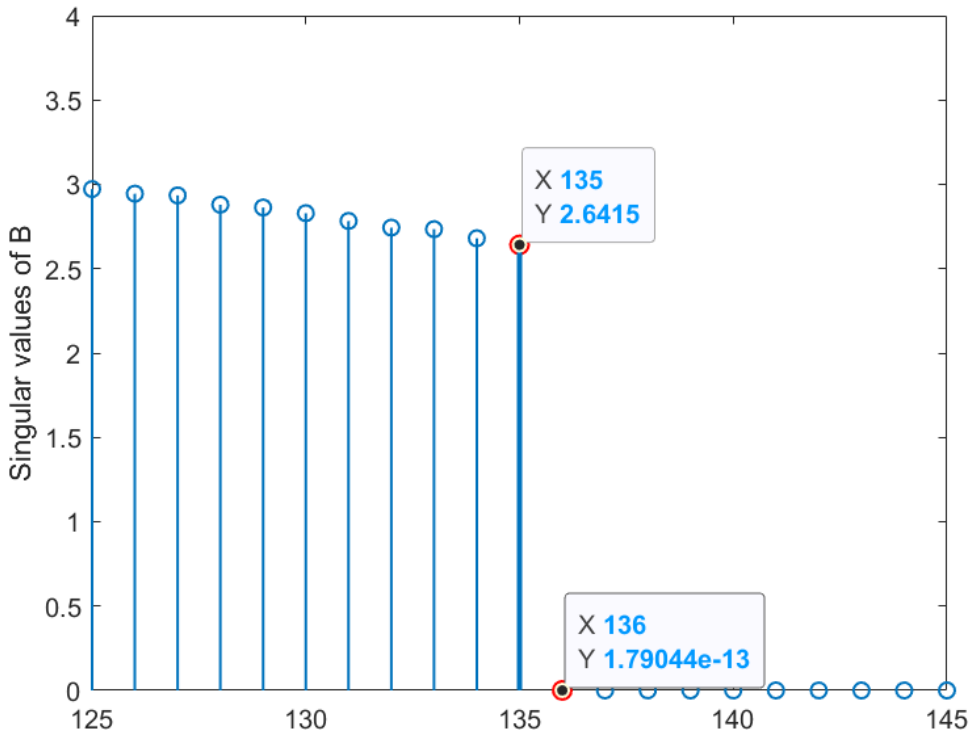

Figure 5.2: Singular values of matrix **B** after the 135^{th} singular value are very close to zero.

It is noted from Figure 5.2 that after the 135^{th} singular value of $\mathbf{B}$, the singular values that follow are not exactly equal to zero, but are very close to zero. The matrix is ill-conditioned since dividing by the singular values $(1/\sigma_i)$ in Eq. (5.8) for σ_i arbitrarily close to zero would lead to extremely large values in the reconstruction. Therefore, the values after the 135^{th} singular value are omitted in the reconstruction of the transmembrane current distribution. Hence, the maximum value that is considered for k in Eq. (5.8) is 135. As the next step, the effect of using different values for k to generate the reconstructed current distribution $\tilde{\mathbf{i}}$ and the changes observed in the resulting backprojection images are analysed.

5.2 Generation of backprojection images

We consider the simulation setup shown in Figure 5.3 for the generation of a backprojection image using the SVD of matrix $\mathbf{B}$ and for drawing a comparison with the backprojection images generated in the previous chapter using the backprojection operator $\mathbf{B}^T$. The current grid in this setup is located to the right, with an overlap of 1.8 mm with the electrode array. The reconstructed transmembrane current vector is generated using Eq. (5.8) for different values of k. The y-slice from these reconstructions is extracted to be imaged. The plots in Figure 5.4 show the resulting backprojection images generated for three values of k taken to be 5, 30 and 135.

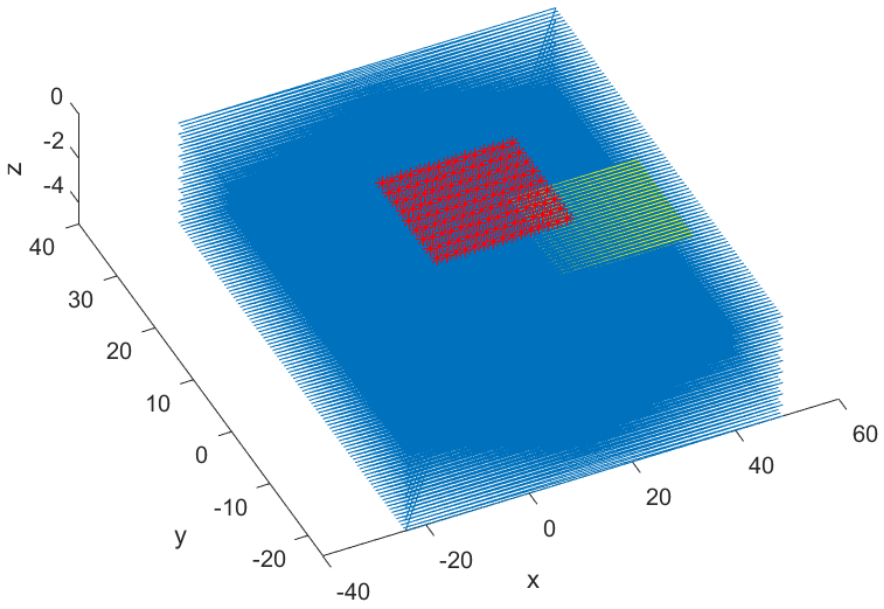

Figure 5.3: Simulation setup

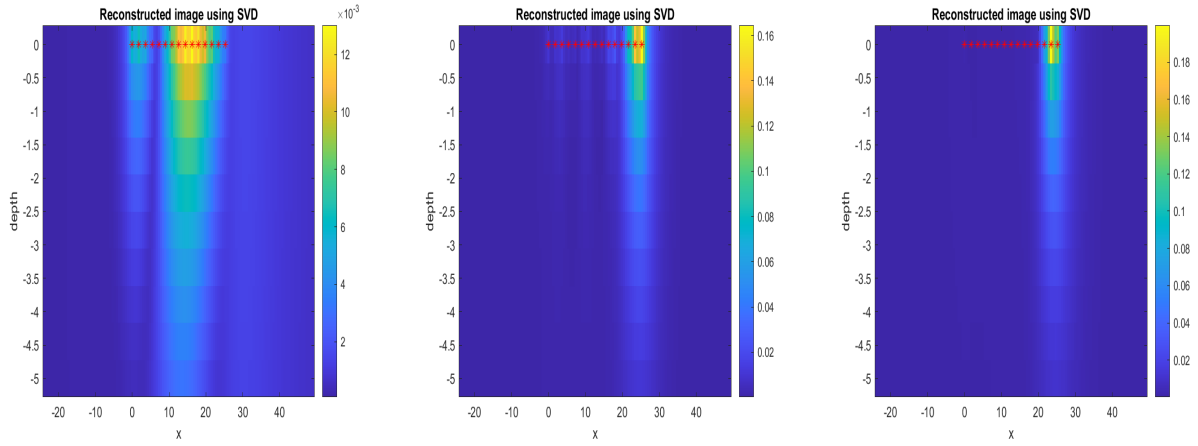

(a) k=5 (b) k=30 (c) k=135

Figure 5.4: Backprojection images obtained by solving Eq. (5.8) for different values of k

For the higher values of k, the backprojection image gives a clear distinct peak with minimal blurring to indicate the location of the atrial activity. The peak is found to coincide with the point where the overlap between the current grid and the electrode array begins. This gives an indication of the location of the current grid with respect to the known electrode array placement. The distinct peak is observed from the instance when $k = 30$. This makes the method computationally less complex as the knowledge of all the singular values of matrix $\mathbf{B}$ is not required in order to obtain an estimate for the location of the atrial activity along the x-direction. Additionally, it is observed that as the value of k is increased, there is reduced blurring around the peak, giving a much clearer estimate for the backprojection image compared to the use of only $\mathbf{B}^T$ as the backprojection operator in Section 4.1.2. The computation is carried out through the use of the SVD and the action of the inverse as shown in Eq. (5.2) has been taken into account while determining the backprojection image in this case, without the need for computing the inverse of the large matrix $\mathbf{B}$ explicitly. The MATLAB code for the case when k=135 takes 43 seconds to run on a PC with an i7 core processor.

Figure 5.5 shows a modified simulation setup where the current grid is displaced to the left with an overlap of 1.8mm with the electrode array. The backprojection images generated for this modified setup using Eq. (5.8) for three different values of k are presented in Figure 5.6. It is noted that the results give an indication of the location of the current grid that has now been displaced to the left. Similar to the results observed in Figure 5.4, the blurring around the peak is minimised as the value of k in Eq. (5.8) is increased.

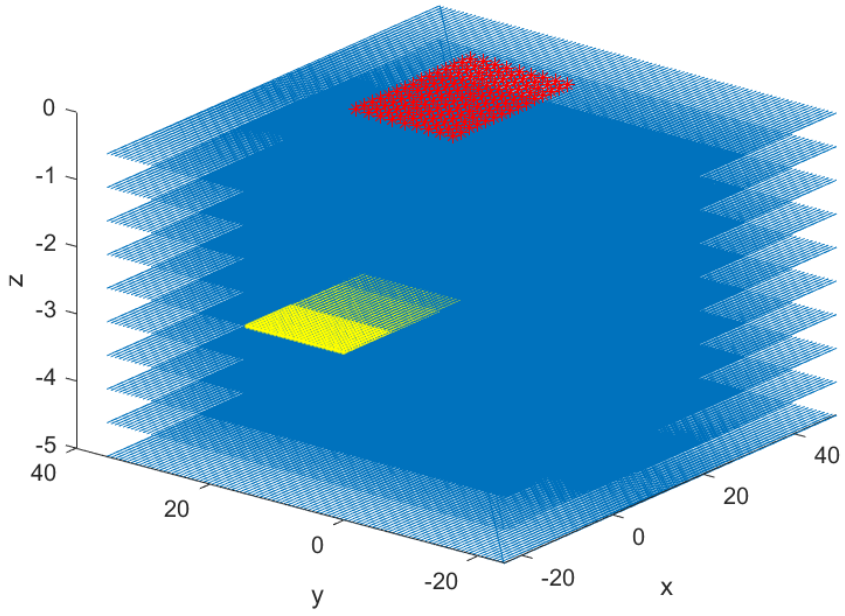

Figure 5.5: Modified Simulation setup

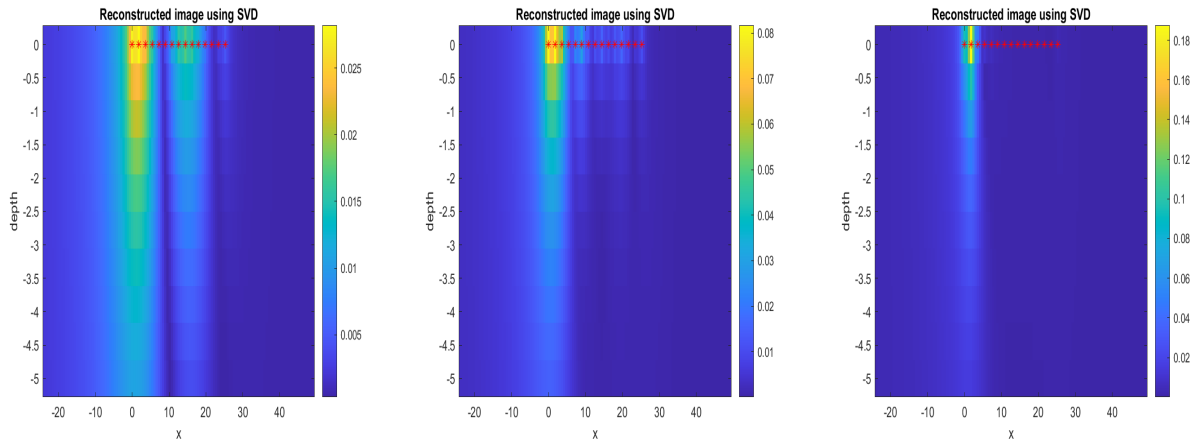

(a) k=5 (b) k=30 (c) k=135

Figure 5.6: Backprojection images obtained by solving Eq. (5.8) for different values of k

Performing a reduced SVD of the **B** matrix is beneficial as it gives a more distinct peak to indicate the location of the current grid with respect to the electrode array used for measurement. The method is also fast and not computationally complex, making it a feasible approach to get an estimate of the atrial activity location within the volume

domain. However, a limitation of the backprojection images generated using this method compared to the images generated in Section 4.1.3 is that the peak observed is very confined and the width of the current grid is not captured in the images generated using the reduced SVD although the localization of the peak to indicate the start of the overlap between the current grid and the electrode array is more accurate. In the backprojection images in Section 4.1.3, the width of the current grid was indicated in the resulting images giving an estimate of the width of tissue where the irregular atrial activity is prominent. In the reconstruction using the SVD, the width information is lost but a more accurate estimate of the point where the current grid begins with reference to the location of the electrode array is obtained. Hence, further analysis of the tissue surrounding this estimate would have to be carried out to guide catheter placements in ablation procedures and improve the success rate of eliminating AF triggers.

6 Conclusion and Future Work

6.1 Summary

In this thesis, an attempt has been made to obtain a visual estimate of irregular electrical activity distribution in a volume domain of heart tissue. The main contributions of the thesis can be summarized as follows:

- An efficient and computationally fast imaging method has been proposed with the use of backprojection images to obtain a visual estimate of the x and y coordinate information of the region where irregular atrial activity is prominent in a volume of heart tissue. Epicardial electrogram measurements obtained by placing an electrode array on the surface of the heart are used as the basis for reconstructing the transmembrane current distribution in a given volume.
- A different placement and orientation of the electrode array is introduced that provides an estimate of the depth of the atrial activity from the surface.
- The ability of the backprojection images to distinguish between closely spaced regions of irregular electrical activity to identify potential AF triggers has been introduced.
- The use of Singular Value Decomposition (SVD) has been proposed to improve the accuracy of localization of the region where irregular atrial activity is prominent while ensuring that the imaging is not computationally complex. This makes the imaging method simple enough for medical experts to visually estimate the site of irregular activity and further analyze the identified areas for AF triggers.

6.2 Discussion

Given the contributions in the thesis, the open discussion points and limitations observed in the proposed methods are reflected upon in this section.

An important point to consider is that the imaging method presented in Chapter 4 for determining the x and y coordinate information of the irregular atrial activity location makes use of epicardial electrogram readings whereas the depth estimation relies on readings obtained by placing the electrode array within the volume of cardiac tissue. While the intra-operative procedure for high resolution atrial mapping and acquiring of epicardial electrogram data is clinically established in [20], the feasibility of the depth estimation method in a clinical setting has to be determined.

Secondly, performing the SVD of the inverse distances matrix and reconstructing the transmembrane current distribution by making use of the singular values in Chapter 5 gives a more accurate estimate of the coordinate where the current grid starts with respect to

the electrode array. The reconstruction is also computationally fast and does not require an explicit computation of the inverse of the large inverse distances matrix. However, this method generates a narrow peak that does not incorporate the width estimate of the current grid. Hence, there is a trade-off between the accuracy of the localization and the need for further analysing the tissue surrounding the estimate due to lack of the width information.

6.3 Future Work

As an extension to this work, the following research directions can be explored:

1. Optimization algorithms for more accurate location estimates: The visual estimates obtained using the proposed backprojection imaging method in this thesis can be used as an initial estimate for the location of atrial activity. The initial estimate can be further optimized by applying gradient descent based optimization algorithms such as Newton's method.
2. Validation with clinical data: The analysis carried out in this research was restricted to electrogram data from a simulated heterogeneous grid of cardiac tissue with zones of reduced and no conduction. A next step would be validating the results obtained for the visual estimates by using epicardial electrogram readings recorded in clinical practice by placing an electrode array to record the potential on the surface of the heart during open heart surgery for a patient exhibiting symptoms of paraoxysmal or permanent AF.
3. Analysing estimated regions for the precise mechanism causing AF: Section 2.2.1 gave an overview of the possible underlying mechanisms that give rise to the irregular heart beat that is characteristic of AF. Once a region of irregular activity has been identified using the visual estimate generated by the imaging method proposed in this thesis, the region can be analysed for the presence of the AF trigger. For example, the presence of rotor core positions can be detected using phase mapping and Convolutional Neural Networks (CNNs) [39], [40].
4. Integration with other imaging modalities: The study of underlying AF mechanisms can be guided by the use of real-time MRI for the assessment of the diseased tissue. Moreover, the mapping and ablation procedures can benefit from MRI-guided electrophysiology [41]. The mapping technique proposed in this thesis combined with imaging modalities such as a cardiac MRI can provide a more comprehensive understanding of the location of the irregular atrial activity and identification of AF triggers that need to be ablated. The imaging can be also be extended to incorporate electrogram readings acquired from multiple electrode arrays placed over the entire epicardial surface at different orientations to give a holistic estimate of the regions in the atria that are responsible for the initiation of AF.

Bibliography

[1] I. C. V. Gelder and M. E. Hemels, "The progressive nature of atrial fibrillation: A rationale for early restoration and maintenance of sinus rhythm," *Europace*, vol. 8, no. 11, pp. 943–949, 2006.

[2] S. Colilla, A. Crow, W. Petkun, D. E. Singer, T. Simon, and X. Liu, "Estimates of current and future incidence and prevalence of atrial fibrillation in the u.s. adult population," *The American journal of cardiology*, vol. 112, no. 8, pp. 1142–1147, 2013.

[3] UMCG, *€2.5 million heart foundation grant for atrial fibrillation research*, `https://umcgresearch.org/w/%E2%82%AC2.5-million-heart-foundation-grant-for-atrial-fibrillation-research` [Accessed: 02/05/2023].

[4] C. T. January, L. S. Wann, J. S. Alpert, *et al.*, "2014 aha/acc/hrs guideline for the management of patients with atrial fibrillation: A report of the american college of cardiology/american heart association task force on practice guidelines and the heart rhythm society," *Journal of the American College of Cardiology*, vol. 64, no. 21, e1–e76, 2014.

[5] National Heart Lung & Blood Institute, *Atrial fibrillation-types*, `https://www.nhlbi.nih.gov/health/atrial-fibrillation/types` [Accessed: 02/05/2023], 2022.

[6] Stanford Health Care, *Breakthrough mapping technology helps target treatment of atrial fibrillation*, `https://stanfordhealthcare.org/campaigns/atrial-fibrillation-firm`[Accessed: 03/05/2023].

[7] John Hopkins Medicine, *Anatomy and function of the heart's electrical system*, `https://www.hopkinsmedicine.org/health/conditions-and-diseases/anatomy-and-function-of-the-hearts-electrical-system` [Accessed: 02/05/2023].

[8] A. G. Kléber and Y. Rudy, "Basic mechanisms of cardiac impulse propagation and associated arrhythmias," *Physiological reviews*, vol. 84, no. 2, pp. 431–488, 2004.

[9] J. Malmivuo and R. Plonsey, *Bioelectromagnetism: Principles and Applications of Bioelectric and Biomagnetic Fields*. Oxford University Press, 1995.

[10] Mayo Clinic, *Heart arrhythmia*, `https://www.mayoclinic.org/diseases-conditions/heart-arrhythmia/symptoms-causes` [Accessed: 03/05/2023].

[11] M. K. Chung, L. L. Eckhardt, L. Y. Chen, H. M. Ahmed, R. Gopinathannair, J. A. Joglar, P. A. Noseworthy, Q. R. Pack, P. Sanders, and K. M. Trulock, "Lifestyle and risk factor modification for reduction of atrial fibrillation: A scientific statement from the American Heart Association," *Circulation*, vol. 141, no. 16, e750–e772, 2020.

[12] R. G. Hart and J. L. Halperin, "Atrial fibrillation and stroke: concepts and controversies," *Stroke*, vol. 32, no. 3, pp. 803–808, 2001.

[13] M. S. Guillem, A. M. Climent, M. Rodrigo, F. Fernández-Avilés, F. Atienza, and O. Berenfeld, "Presence and stability of rotors in atrial fibrillation: evidence and therapeutic implications," *Cardiovascular research*, vol. 109, no. 4, pp. 480–492, 2016.

[14] D. E. Krummen, V. Swarup, and S. M. Narayan, "The role of rotors in atrial fibrillation," *Journal of thoracic disease*, vol. 7, no. 2, pp. 142–151, 2015.

[15] J. W. Waks and M. E. Josephson, "Mechanisms of Atrial Fibrillation - Reentry, Rotors and Reality," *Arrhythmia electrophysiology review*, vol. 3, no. 2, pp. 90–100, 2014.

[16] N. de Groot, L. van der Does, A. Yaksh, *et al.*, "Direct Proof of Endo-Epicardial Asynchrony of the Atrial Wall During Atrial Fibrillation in Humans," *Circulation. Arrhythmia and electrophysiology*, vol. 9, no. 5, e003648, 2016.

[17] N. F. Marrouche, J. Brachmann, D. Andresen, *et al.*, "Catheter ablation for atrial fibrillation with heart failure," *New England Journal of Medicine*, vol. 378, no. 5, pp. 417–427, 2018.

[18] John Hopkins Medicine, *Atrial fibrillation ablation*, `https://www.hopkinsmedicine.org/health/treatment-tests-and-therapies/atrial-fibrillation-ablation` [Accessed: 09/05/2023].

[19] V. Jacquemet, A. V. Oosterom, J. Vesin, and L. Kappenberger, "Analysis of electrocardiograms during atrial fibrillation," *IEEE Engineering in Medicine and Biology Magazine*, vol. 25, no. 6, pp. 79–88, 2006.

[20] A. Yaksh, L. J. van der Does, C. Kik, P. Knops, F. B. Oei, P. C. van de Woestijne, J. A. Bekkers, A. J. Bogers, M. A. Allessie, and N. M. de Groot, "A novel intra-operative, high-resolution atrial mapping approach," *Journal of interventional cardiac electrophysiology : an international journal of arrhythmias and pacing*, vol. 44, no. 3, pp. 221–225, 2015.

[21] M. Sun, "Modelling and analysis of atrial epicardial electrograms an approach based on graph signal processing and confirmatory factor analysis," Ph.D. dissertation, Delft University of Technology, 2022.

[22] N. V. V. Jacquemet and C. Henriquez, "Study of atrial arrhythmias in a computer model based on magnetic resonance images of human atria," *Chaos: An Interdisciplinary Journal of Nonlinear Science*, vol. 32, no. 3, pp. 754–763, 2002.

[23] H. Bernus, O. Cherry, and R. Clayton, "Models of cardiac tissue electrophysiology: progress, challenges and open questions," *Progress in biophysics and molecular biology*, vol. 104, no. 1-3, pp. 22–48, 2011.

[24] M. Potse, B. Dube, J. Richer, A. Vinet, and R. M. Gulrajani, "A Comparison of Monodomain and Bidomain Reaction-Diffusion Models for Action Potential Propa-

gation in the Human Heart," *IEEE Transactions on Biomedical Engineering*, vol. 53, no. 12, pp. 2425–2435, 2006.

[25] M. Courtemanche, R. Ramirez, and S. Nattel, "Ionic mechanisms underlying human atrial action potential properties: Insights from a mathematical model.," *The American journal of physiology*, vol. 275, no. 1, H301–H321, 1998.

[26] B. Abdi, "Atrial fibrillation fingerprinting," Ph.D. dissertation, Delft University of Technology, 2021.

[27] "Cancellation of ventricular activity in unipolar endocardial recordings during atrial fibrillation," in *2013 ISSNIP Biosignals and Biorobotics Conference: Biosignals and Robotics for Better and Safer Living (BRC)*, 2013, pp. 1–6.

[28] J. S. E. Byrom and L. McCarthy, "Computer detection of atrioventricular dissociation from surface electrocardiograms during wide qrs complex tachycardias," *Circulation*, vol. 72, no. 5, pp. 1028–1036, 1985.

[29] J. Rieta, F. Hornero, R. Alcaraz, and D. Moratal, "Ventricular artifacts cancellation from atrial epicardial recordings in atrial tachyarrhythmias," in *Annual International Conference of the IEEE Engineering in Medicine and Biology Society.*, 2007, pp. 6504–6507.

[30] J. Rieta and F. Hornero, "Comparative study of methods for ventricular activity cancellation in atrial electrograms of atrial fibrillation," *Physiological measurement*, vol. 28, no. 8, pp. 925–936, 2007.

[31] B. Abdi, R. C. Hendriks, A. van der Veen, and N. De Groot, "Ventricular activity signal removal in atrial electrograms of atrial fibrillation," in *Biosignals*, 2019, pp. 179–184.

[32] T. Moree, M. S. van Schie, N. M. de Groot, and R. C. Hendriks, "Estimation of the atrial activity from electrograms: A beamforming perspective," in *2022 Computing in Cardiology (CinC)*, Tampere, Finland, 2022, pp. 1–4.

[33] B. Abdi, R. C. Hendriks, A.-J. van der Veen, and N. M. de Groot, "A compact matrix model for atrial electrograms for tissue conductivity estimation," *Computers in Biology and Medicine*, vol. 107, pp. 284–291, 2019.

[34] B. Abdi, A.-J. van der Veen, N. M. de Groot, and R. C. Hendriks, "Local activation time estimation in fractionated electrograms of cardiac mappings," in *2019 41st Annual International Conference of the IEEE Engineering in Medicine and Biology Society (EMBC), IEEE*, 2019, pp. 285–288.

[35] R. Plonsey and R. Barr, *Bioelectricity: a quantitative approach*. Springer Science Business Media, 2007.

[36] S. Rolf, G. Hindricks, P. Sommer, S. Richter, A. Arya, A. Bollmann, J. Kosiuk, and E. Koutalas, "Electroanatomical mapping of atrial fibrillation: Review of the current techniques and advances," *Journal of atrial fibrillation*, vol. 7, no. 4, 2014.

[37] H. Mori, R. Kato, Y. Ikeda, *et al.*, "The influence of the electrodes spacing of a mapping catheter on the atrial voltage substrate map," *Journal of Cardiology*, vol. 72, no. 5, pp. 434–442, 2018.

[38] J. Liu, X. Zhang, Y. Liu, *et al.*, "Intrinsically stretchable electrode array enabled in vivo electrophysiological mapping of atrial fibrillation at cellular resolution.," *Proceedings of the National Academy of Sciences of the United States of America*, vol. 117, no. 26, pp. 14 769–14778. 2020.

[39] P. Podziemski, S. Zeemering, P. Kuklik, A. van Hunnik, B. Maesen, J. Maessen, H. J. Crijns, S. Verheule, and U. Schotten, "Rotors Detected by Phase Analysis of Filtered, Epicardial Atrial Fibrillation Electrograms Colocalize With Regions of Conduction Block," *Circulation. Arrhythmia and electrophysiology*, vol. 11, no. 10, e005858, 2018.

[40] J. Lebert, N. Ravi, F. H. Fenton, and J. Christoph, "Rotor Localization and Phase Mapping of Cardiac Excitation Waves Using Deep Neural Networks.," *Frontiers in physiology*, vol. 12, 2021.

[41] R. K. Mukherjee, H. Chubb, S. Roujol, R. Razavi, and M. D. O'Neill, "Advances in Real-Time MRI-Guided Electrophysiology," *Current cardiovascular imaging reports*, vol. 12, no. 2, 2019.